

## Generation and evaluation of an artificial optical signal based on X-ray measurements for bubble characterization in fluidized beds with vertical internals

Schillinger, F.; Schildhauer, T. J.; Maurer, S.; Wagner, E.; Mudde, R. F.; van Ommen, J. R.

**DOI**

[10.1016/j.ijmultiphaseflow.2018.03.002](https://doi.org/10.1016/j.ijmultiphaseflow.2018.03.002)

**Publication date**

2018

**Document Version**

Final published version

**Published in**

International Journal of Multiphase Flow

**Citation (APA)**

Schillinger, F., Schildhauer, T. J., Maurer, S., Wagner, E., Mudde, R. F., & van Ommen, J. R. (2018). Generation and evaluation of an artificial optical signal based on X-ray measurements for bubble characterization in fluidized beds with vertical internals. *International Journal of Multiphase Flow*, 107, 16-32. <https://doi.org/10.1016/j.ijmultiphaseflow.2018.03.002>

**Important note**

To cite this publication, please use the final published version (if applicable). Please check the document version above.

**Copyright**

Other than for strictly personal use, it is not permitted to download, forward or distribute the text or part of it, without the consent of the author(s) and/or copyright holder(s), unless the work is under an open content license such as Creative Commons.

**Takedown policy**

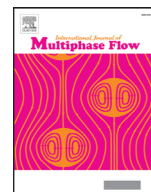
Please contact us and provide details if you believe this document breaches copyrights. We will remove access to the work immediately and investigate your claim.

***Green Open Access added to TU Delft Institutional Repository***

***'You share, we take care!' – Taverne project***

**<https://www.openaccess.nl/en/you-share-we-take-care>**

Otherwise as indicated in the copyright section: the publisher is the copyright holder of this work and the author uses the Dutch legislation to make this work public.



# Generation and evaluation of an artificial optical signal based on X-ray measurements for bubble characterization in fluidized beds with vertical internals



F. Schillinger<sup>a</sup>, T.J. Schildhauer<sup>a,\*</sup>, S. Maurer<sup>a</sup>, E. Wagner<sup>b</sup>, R.F. Mudde<sup>b</sup>, J.R. van Ommen<sup>b</sup>

<sup>a</sup> Paul Scherrer Institut, PSI, 5232 Villigen, Switzerland

<sup>b</sup> Delft University of Technology, Van der Maasweg 9, 2629 HZ Delft, The Netherlands

## ARTICLE INFO

### Article history:

Received 22 October 2017

Revised 25 February 2018

Accepted 3 March 2018

Available online 6 March 2018

### Keywords:

Bubbling fluidized bed

Measurement methods

X-ray

Optical

Bubble properties

Monte Carlo simulation

## ABSTRACT

The performance of fluidized bed reactors strongly depends on the bubble behavior, for which reason knowledge concerning the bubble properties is important for modeling and reactor optimization. X-ray measurements can be used to characterize bubbles within the cross-section of a fluidized bed on a laboratory scale, but cannot easily be extended to hot, pressurized large scale plants. For future measurements at hot conditions in a fluidized bed methanation reactor, we have developed an optical probing system that can be employed under these conditions. However, optical sensors are only able to investigate the local fluidization patterns at a defined position in the bed. The objective of this study is to characterize differences in bubble properties between local optical measurements and an X-ray tomography method that is able to detect bubbles over the entire cross-section. Therefore, an artificial optical signal is created out of existing hydrodynamic X-ray measurement data obtained at a cold flow model of a pilot scale methanation reactor. The determined bubble properties of both methods (i.e. evaluation of the derived artificial optical probe signal and image reconstruction based on the evaluation of original X-ray tomographic data) are compared with regard to the bubble rise velocity and the bubble size (for the X-ray method) or pierced chord length (for the optical evaluation method), respectively. The comparison shows that for the evaluation of the optical probe data, statistical effects have to be considered carefully. The detected mean chord length of the optical method does not immediately correspond to the mean bubble size determined by the X-ray method. Moreover, also differences regarding the bubble rise velocity were detected for some fluidization states. The reason for the discrepancies between both methods could be identified and corrected, amongst others by means of a Monte Carlo simulation in which rising bubbles in a fluidized bed were simulated and characterized by a local virtual optical sensor.

© 2018 Elsevier Ltd. All rights reserved.

## 1. Introduction

The hydrodynamics of a fluidized bed have to be understood for a proper design and scale-up of fluidized bed reactors. For this purpose, hydrodynamic properties like the bubble hold-up, the bubble size or the bubble rise velocity (BRV) have to be measured. A wide range of different measurement techniques are available. Which ones are preferred, strongly depends on the application and the required information that becomes accessible by the individual measurement techniques (Asegehegn et al., 2011; Rautenbach et al., 2013; van Ommen and Mudde, 2007; Verma et al., 2014). The measurement techniques can be subdivided into intrusive and non-intrusive methods. Optical sensors are often used as intru-

sive probes since they are easy to construct, have a reasonable price and their application has already been proven for a long time (Acosta-Iborra et al., 2011; Glicksman et al., 1987; Rüdüsüli et al., 2012a; Whitehead et al., 1967). Due to their intrusive character, it cannot be excluded that the flow pattern gets disturbed by the sensor. To deal with this issue, the influence of intrusive probes on the flow structure in fluidized bed systems is investigated in Bai et al. (2010), Maurer et al. (2015a), Tebianian et al. (2015,2016), Whitemarsh et al. (2016). The possibility to design an optical sensor in a way that the flow structure is almost not influenced by the intrusive character of the sensor is shown in Maurer (2015), Maurer et al. (2015a), and Whitemarsh et al. (2016).

A significant drawback of optical probes is the fact that they only deliver local information of the fluidization state like the pierced chord length of a bubble instead of the entire bubble diameter. Expensive, non-intrusive methods, such as X-ray or electrical capacitance tomography, may provide information of the flu-

\* Corresponding author.

E-mail address: [tilman.schildhauer@psi.ch](mailto:tilman.schildhauer@psi.ch) (T.J. Schildhauer).

idization state over the entire cross section and gather the bubble diameter, the hydraulic bubble diameter and the position of the center of gravity (Maurer et al., 2015a). However, these measurement methods cannot be easily implemented at industrial scale (Liu et al., 2010).

If heat has to be removed out of the reactor in the case of exothermic reactions or to supply endothermic reactions with the required amount of heat, a heat transfer system which consists of a vertical heat exchanger tubes has to be integrated inside the reactor. For the case of hydrodynamic investigations of cold-flow fluidized beds, the vertical heat exchanger tubes are replaced by vertical internals with the same geometry. Investigations on the influence of vertical heat exchanger tubes on the hydrodynamic behavior have already been conducted in (Maurer et al., 2016,2015b,c) and simulations based on a two fluid model in Verma et al. (2016). A new correlation for the bubble size and bubble rise velocity which considers the presence of vertical internals was published in Maurer et al. (2016). These studies have shown that vertical internals strongly influence the bubble properties. One of the main findings was the fact that the bubble shape deviates to a larger extent from a spherical shape if vertical internals are present compared to a configuration without internals.

If the geometry of the bubbles is known and can be described mathematically, methods to convert the chord length distribution of the pierced bubbles into a bubble size distribution of all bubbles exist in literature (Clark and Turton, 1988; Rüdiss-üli et al., 2012b; Santana and Macias-Machin, 2000). Moreover, Sobrino et al. (2015) showed for a two fluid model simulation of a three-dimensional bubbling fluidized bed (BFB) without vertical internals that the pierced chord length distribution can be confidently transferred into an equivalent bubble volume diameter distribution by means of mathematic methods.

However, these methods are not suitable for systems in which the bubble shape cannot be described by a simple mathematical equation as it is the case for the investigated fluidized bed with vertical internals. In the scope of this study, the relation between the pierced chord length and the volume equivalent bubble diameter based on experimental data is investigated for the first time.

At the Paul Scherrer Institute (PSI), an intrusive optical measurement system was developed to detect bubbles in a bubbling fluidized bed reactor under hot, pressurized and reactive conditions for the case of a methanation reactor. It should be pointed out that no X-ray measurements will be available to measure the hydrodynamics under these conditions.

The measurement principle of an optical sensor is based on the reflection of light by the bed material. Laser light is fed into the optical sensor which is composed of optical fibers. The light enters the fluidized bed at the probe tip. For the case that no bubble is in front of the probe tip, light is reflected to a large extent by the white bed material ( $\text{Al}_2\text{O}_3$ ). If there is a bubble in front of the sensor significantly less light is reflected. The amount of reflected light is analyzed by a phototransistor that generates the voltage signal which is used for further evaluation. The measurement principle is schematically depicted in Fig. 1.

The intention of the present study is to work out a methodology to describe the relation of the bubble properties that are determined by means of optical measurements to the bubble properties that are determined with X-ray measurements for a fluidized bed with vertical internals. Based on these results, future optical measurements can be interpreted more precisely. In order to compare the bubble properties determined by both methods, the data sets of the X-ray measurements are used as basis to generate an artificial optical signal. By generating a fictitious optical signal out of X-ray data, one can ensure that the data base for the evaluation of the optical signal is identical to the data base that is used for the evaluation of the X-ray signal. A sequential performance of optical

and X-ray measurements could not guarantee the condition of analyzing the same fluidization state. A parallel performance of X-ray measurements and optical measurements is not possible since the optical sensor which is made out of steel influences the X-ray signal. Moreover, if we used a real optical probe for this comparison, other effects like the disturbance of the flow pattern by the optical sensor could not be quantified. Hence, the generated artificial optical data set corresponds to the signal of a virtual and perfectly working optical sensor that is located at defined positions in the column that has no influence on the actual flow structure.

Systematic differences between both methods concerning the determined bubble size and the bubble rise velocity were detected in the scope of this work. By applying the conclusions of this paper, it is possible to assess future results of hydrodynamic measurements in bubbling fluidized beds for which only intrusive optical measurements are available. The underlying raw data sets of X-ray measurements which are used for this study are available as part of a previous work in a cold-flow bubbling fluidized bed that has been conducted in the scope of Maurer (2015). In summary, it can be stated that the explicit goal of this methodological paper is to compare the optical evaluation method with the X-ray evaluation method to determine the bubble properties with the particularity that both data sets originate from the identical measurement campaign. A detailed hydrodynamic characterization of bubbling fluidized beds with vertical internals is shown in Maurer (2015), Maurer et al. (2016,2015b,2014), Schillinger et al. (2017) and is therefore not in the focus of this study.

## 2. Theoretical background of the two-phase model

The classical approach to describe the behavior of a bubbling fluidized bed is the two phase model which is depicted in Fig. 2. The idea of this model is to separate the total gas flow entering the column ( $u$ ) into a part that flows through the bubble phase ( $u_{bub.}$ ) and a part that flows through the dense phase ( $u_d$ ) (Davidson and Harrison, 1966). The local bubble hold-up  $\varepsilon_b$  is calculated by the area that is covered by bubbles divided by the free cross-section of the column.

A more detailed theory was proposed by Grace and Clift (1974) who stated that the gas flow in the bubble phase can be further divided into the superficial gas velocity through the bubble phase ( $v_b$ ) which corresponds to the volume flow of gas that rises in the form of bubbles with regard to the entire cross-section at one measurement height (see Eq. (1)) and into a bubble throughflow ( $u_{tf}$ ). A balance of the gas phase leads to Eq. (2) (Gogolek and Grace, 1995). However, the bubble throughflow is usually negligible.

$$v_b = \frac{\dot{V}_b}{A} \quad (1)$$

$$u = v_b + \varepsilon_b u_{tf} + (1 - \varepsilon_b) u_d \quad (2)$$

A dimensionless parameter  $\psi$  (see Eq. (3)) was introduced in Hillgardt and Werther (1985) to describe the deviation of the superficial gas velocity through the bubble phase from the classical two-phase theory which states that the entire gas flow above the minimum fluidization flows through the bed in the form of bubbles.

$$v_b = \psi \cdot (u - u_{mf}) \quad (3)$$

The parameter  $\psi$  can be determined based on a correlation (see Eq. (4)) in dependence of the column diameter  $d_t$  and the height above the distributor plate  $h$  for particles with Geldart B classification.

$$\psi = \begin{cases} 0.67 & h/d_t < 1.7 \\ 0.51 \cdot \sqrt{h/d_t} & 1.7 < h/d_t < 4 \\ 1 & h/d_t > 4 \end{cases} \quad (4)$$

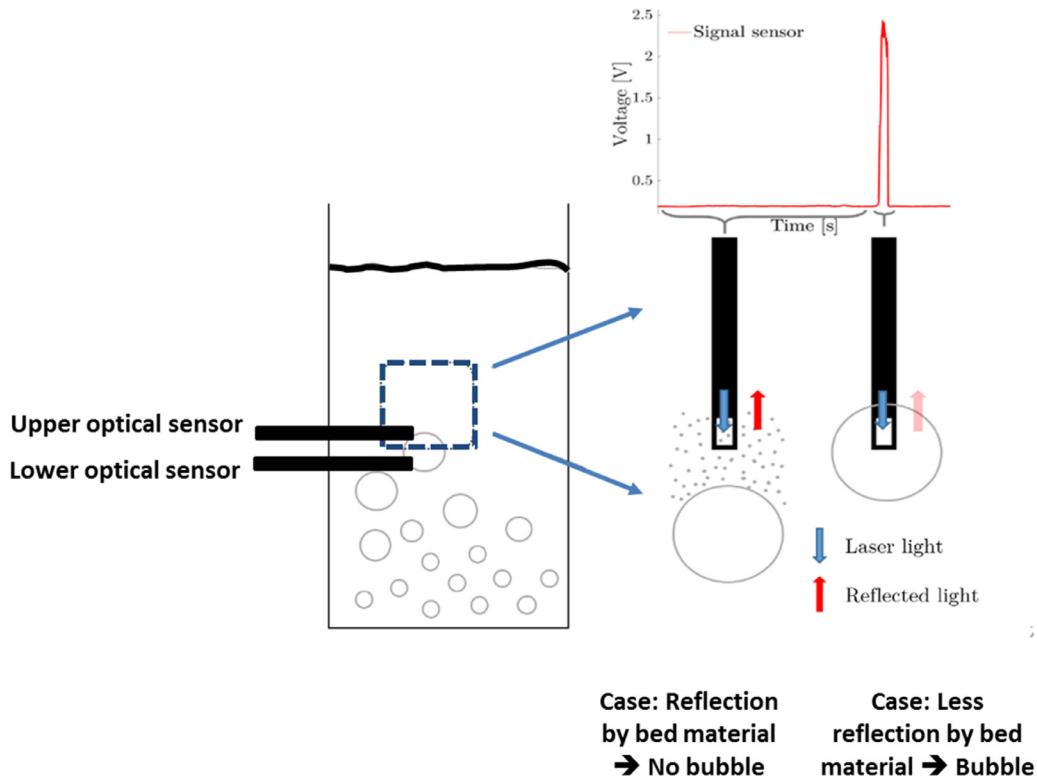


Fig. 1. Measurement principle of the optical sensor.

Combination of Eqs. (2) and (3) and the information given in Fig. 2 leads to Eq. (5) which can be used to calculate the superficial gas velocity through the dense phase. The bubble throughflow ( $u_b$ ) is neglected.

$$u_d = \frac{u - \psi (u - u_{mf})}{1 - \varepsilon_b} \quad (5)$$

### 3. Experimental setup

The experiments were conducted in a cold flow model at ambient temperature and pressure.  $\gamma$ -Alumina in the range of Geldart A/B (Werther, 2007) with a Sauter mean diameter of 289  $\mu\text{m}$  and a particle density of 1350  $\text{kg}/\text{m}^3$  was used as bed material. Gas distribution was achieved by a porous sintered metal plate with a thickness of 3 mm and a mean pore size of 10  $\mu\text{m}$  since this type can also be used at high temperatures and under pressure. The column was filled with bed material up to a height of 60 cm. The minimum fluidization velocity  $u_{mf}$  which corresponds to superficial gas velocity at which the bed begins to fluidize was determined to be 3 cm/s in Rüdüsüli (2012). The fluidization number  $u/u_{mf}$  stands for the ratio between the total gas velocity and the gas velocity at incipient fluidization. Round, square-arranged internals are placed inside the column with an inner diameter of 22.4 cm as depicted in Fig. 3(a). These internals mimic the heat exchanger tubes in the investigated cold-flow model since they will be required for upcoming experiments in a methanation reactor. The larger internal tubes have a diameter of 2 cm, the smaller ones which are close to the margin of the column have a diameter of 1 cm.

Fig. 4 depicts a schematic drawing of the applied X-ray device for hydrodynamic measurements at the column. The apparatus is composed of three stationary X-ray sources. The measurements were conducted at a X-ray energy of 150 keV and a current of 1 mA. The detection of the X-ray beams takes places at two heights with a vertical distance of 4 cm. At each height, three de-

tektor sets are arranged in a circle around the column. Each detector set consists of 32 detectors that are arranged side by side. The average vertical distance between the X-ray beams reaching the lower and the upper detector set is 18.2 mm (15.5 mm at the inlet of the column and 21 mm at the outlet of the column). The distance between the source and the column center was 714 mm. The distance between the detector set and the column center was 532 mm. The signal strength of each measurement point is converted into a path length occupied by air with a calibration factor that was determined by a seven point calibration. A detailed description of the experimental setup and the measuring device has already been given in Mudde (2011).

All X-ray measurements were conducted for 120 s with a frequency of 2500 Hz. X-ray measurements were completed at fluidization numbers ( $u/u_{mf}$ ) of 3, 4 and 6 at two different bed locations of  $H = 36$  cm and  $H = 56$  cm.

### 4. Methodology

#### 4.1. Determination of bubble properties based on the X-ray evaluation algorithm

The principle of the X-ray measurements is based on measuring the attenuation of the X-ray beams through the bed material before they reach the single detector arrays. The attenuation which is measured at each detector array is converted into a path length occupied by air for each detector array. The conversion factor between the attenuation and the path length occupied by air is based on a 7-point calibration. A detailed description of the calibration process is given in Maurer et al. (2015c).

The mathematical reconstruction of the fluidization state based on the X-ray measurements is conducted with a simultaneous algebraic image reconstruction technique (SART) (Andersen and Kak, 1984) that has already been applied to reconstruct images for the same measurement setup in Maurer et al. (2015c). The

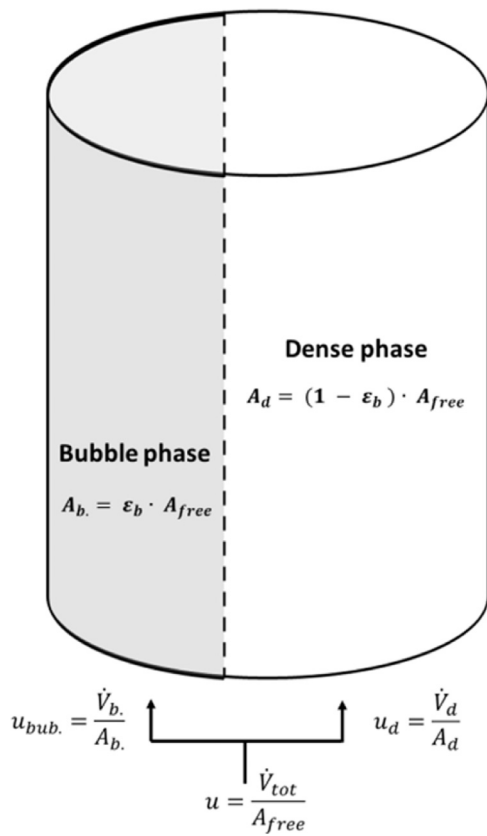


Fig. 2. Schematic view on the classical two-phase model.

present measurement setup enables a resolution of  $55 \times 55$  pixels for the reconstructed images. Three exemplary reconstructed images of the non-threshold filtered fluidization state are given in Fig. 5 in which the location of bubbles is indicated by the grey areas.

The application of the SART algorithm enables a significant reduction of the salt and pepper noise with the drawback of a higher computational effort (Mudde, 2011). Fig. 6 shows the raw signal obtained at one random pixel in the  $55 \times 55$  pixel pattern in which the bubble events can be clearly separated by the dense phase.

Based on this resolution and the column diameter of 22.4 cm, the dimension of a pixel is 0.4 cm x 0.4 cm. A variable pixel size cannot be implemented in the SART image reconstruction for which reason the position of the internals and the margin of the column have to be approximated by pixels of the same size. In total, internals with a diameter of 2 cm are approximated by 21 pixels

and internals with a diameter of 1 cm are approximated by 5 pixels in total (see Fig. 7).

The round column lies centrally in the quadratic array of  $55 \times 55$  pixels as depicted in Fig. 3(c). It has to be mentioned that the positioning of the square arranged internals is twisted by an angle of  $4.9^\circ$  towards the principal axis due to geometrical constraints in the measurement setup. To reduce the computational effort, the mean of ten succeeding measurement points was taken resulting in an effective measurement frequency of 250 Hz.

The output of the image reconstruction process is a matrix with the size of  $[55 \times 55 \times 30,000]$  elements in each case for the upper and lower detector. The matrices include the information of the solid fraction for each pixel as a grey scale between zero and one for all of the 30,000 time increments at the certain measurement height.

For the further data processing, the threshold of the solid fraction was set to 75%, a value that has already been used for the evaluation of X-ray measurements in the scope of Maurer (2015). Above this value, the matrix element is assigned to the dense phase, below the threshold it is assigned to the bubble phase. This leads to a binary matrix filled with zeros and ones which includes the complete information of the fluidization state during the measurement period. An example picture of the reconstructed fluidization state with a resolution of  $55 \times 55$  pixels for a random moment in time is shown in Fig. 3(b). All white pixels (zeros) other than the position of the internals are related to the bubble phase; all black pixels (ones) to the dense phase. The position of the internals as well as the area outside the column is set to zero per definition and excluded from locating bubbles in the evaluation algorithm. It should be noted that the reconstructed fluidization state (see Fig. 3(b)) is derived after applying a threshold filter to the grey-scale images (see Fig. 5) in order to obtain a binary signal. Subsequently, the binary signal of the area inside the column in which no internals are located is inverted.

After applying the threshold, the bubble linking algorithm scans the matrix of all connected structures for which the elements have the value of zero (bubble phase). The outer shell of every independent structure is assigned to a bubble. The shape of a bubble is not influenced by some elements inside which may be assigned to the value of one (emulsion phase) since, for example, if particles are present inside the bubble. The rise velocity of a bubble is calculated by the time span, the center of gravity needs to pass the lower and upper detector array.

By means of this procedure, the volume equivalent bubble diameter and the hydraulic bubble diameter can be determined. The smallest bubble size that can be reconstructed by means of the X-ray evaluation method is influenced by the number of detector arrays and the diameter of the investigated column. The relative

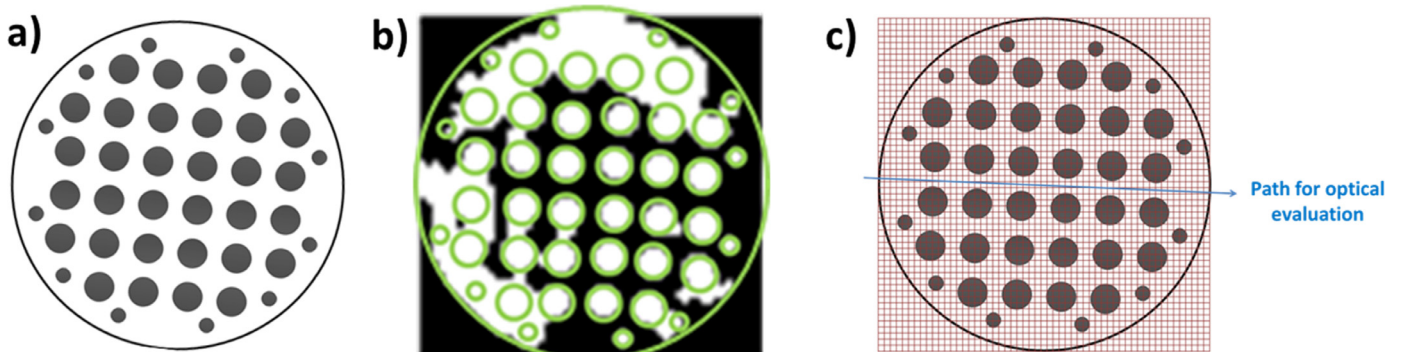


Fig. 3. (a) Cross-section of the column, (b) exemplary reconstructed fluidization state determined by X-ray measurements with overlaid internals, (c) overlaid  $55 \times 55$  pixel pattern for generation of fictitious optical signal (with evaluation path along the centerline of the column).

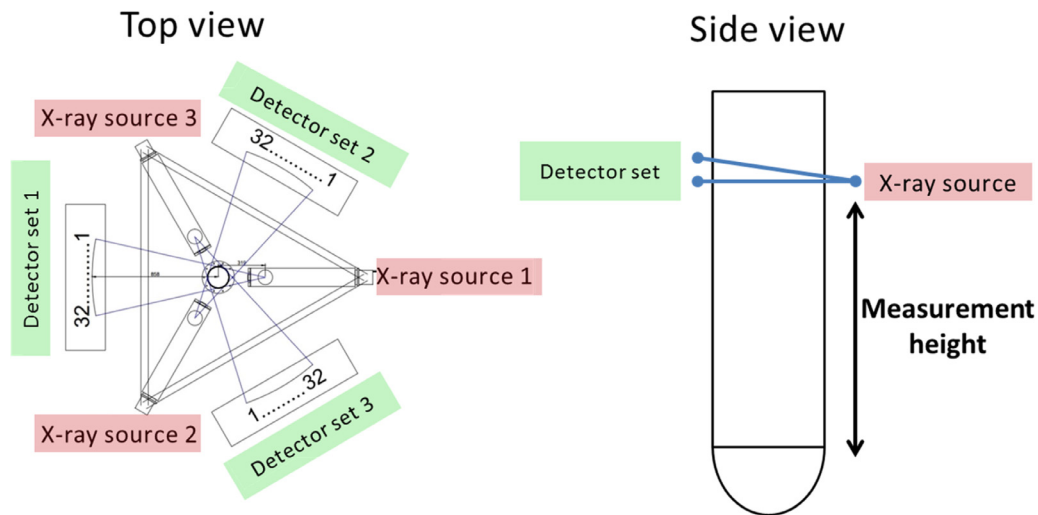


Fig. 4. Top view and side view of the X-ray tomographic setup adapted from (Maurer et al., 2015c).



“White” pixel → Dense Phase / internals

“Grey pixels” → Bubble phase

“Black pixels” → Area outside of the column

Fig. 5. Exemplary reconstructed and non-threshold filtered images of the fluidization state.

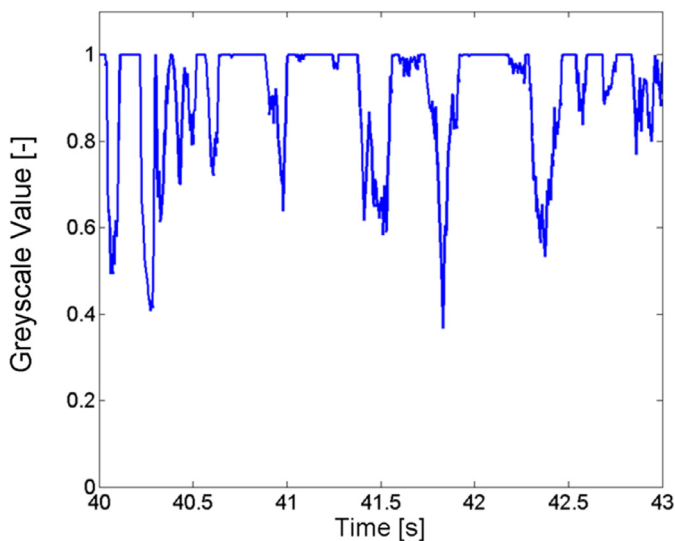


Fig. 6. Signal of grey scale plotted over time for a random pixel in the  $55 \times 55$  pattern.

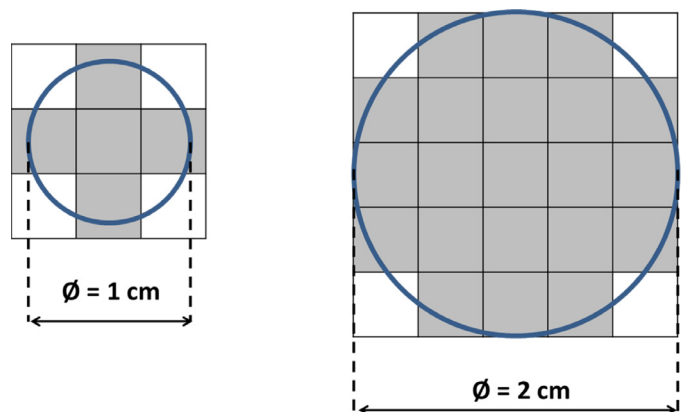


Fig. 7. Approximation of the internals' location by pixels with a size of  $0.4 \text{ cm} \times 0.4 \text{ cm}$ .

accuracy of the SART reconstruction algorithm to determine the bubble size reduces towards smaller bubbles. For example, a bubble with a diameter of 2 cm could be determined with a maximum

accuracy of  $\pm 25\%$  and a bubble with a diameter of 10 cm could be determined with a maximum accuracy of  $\pm 5\%$  in Maurer et al. (2015c). The void fraction of smaller bubbles might be added to the void fraction of larger bubbles in the bubble reconstruction for which reason the average void fraction over the cross-section of the column is quite precise after the reconstruction algorithm has reached convergence.

The image reconstruction based on the SART algorithm may also lead to artefacts that occur as apparent small bubbles since only three X-ray sources are used (Mudde, 2010). The occurrence of artefacts could be reduced by the application of a five point X-ray source as investigated in Mudde et al. (2005). To ensure that the reconstructed bubbles do not originate from an artefact, all bubbles with a chord length smaller than 1.5 cm are excluded from further investigations. Although, it is evident that not every single bubble with a chord length smaller than 1.5 cm is the result of an artefact, small bubbles are uncritical concerning the breakthrough of reactants. One general purpose of this work is to feed a two-phase computer model with experimental data on the bubble behavior to predict the conversion of a bubbling fluidized bed reactor. Neglecting smaller bubbles in a two-phase computer model of a bubbling fluidized bed reactor decreases the calculated conversion. Hence, the calculated conversion describes a worst case scenario of a bubbling fluidized bed reactor without small bubbles. Expectedly, the conversion of a real fluidized bed reactor should be higher than the calculated conversion.

Higher resolutions can be achieved by an increasing number of detector arrays which also enables the detection of smaller bubbles. First results generated by X-ray measurements at a plate detector with a resolution of roughly  $1500 \times 1500$  pixels in the vertical direction are presented in Gomez-Hernandez et al. (2016). A further installation of additional plate detectors would enable a direct 3-dimensional imaging of the bubbles. An algorithm to evaluate the bubble properties resulting from 3-dimensional hydrodynamic measurements is presented in Bakshi et al. (2016). This algorithm shows the advantage that bubbles can be tracked along their trajectories and smaller bubbles are detected with an increased likelihood.

#### 4.2. Determination of bubble properties based on the optical evaluation algorithm

The matrix obtained by the X-ray tomographic reconstruction algorithm (SART) is the basis to create an artificial optical signal. The entire information on the fluidization state at the measurement height is stored in this matrix. Therefore, tracking one position in the matrix over time corresponds to a perfectly working virtual optical sensor which is inserted into the column without influencing the flow structure. The optical signal sequence was sampled at each pixel along the evaluation path separately as shown in Fig. 3(c).

To gain the bubble properties, it is necessary to evaluate both the signal of the lower and upper measurement plane. The evaluation step to assign a signal peak of a bubble which is detected at the lower sensor to the corresponding signal peak of the upper sensor is named the bubble linking step. The average distance of 18.2 mm for the X-ray beams that reach the lower and upper detector arrays is used as vertical distance  $\Delta s$  in Eq. (6). By means of the time difference  $\Delta t$  between the exceedance of the threshold at the lower and the upper sensor, the bubble rise velocity  $u_b$  can be calculated according to Eq. (6). Since the range of the vertical separation for X-ray beams that reach the lower and upper detector arrays is between 15.4 mm and 21 mm (see Fig. 4), the uncertainty concerning the determined bubble rise velocity may be up to 18%

$$u_b = \frac{\Delta s}{\Delta t} \quad (6)$$

The chord length of a bubble is calculated as the product of  $u_b$  and the gapless time period below the threshold  $t_b$  as shown in Eq. (7).

$$d_{\text{chord}} = u_b \cdot t_b \quad (7)$$

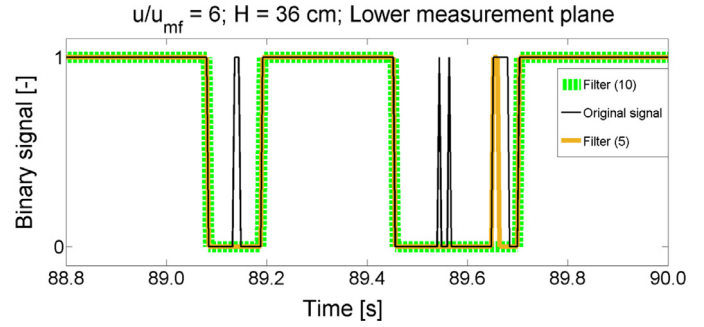


Fig. 8. Effect of filter application on signal for an exemplary time interval at the lower measurement plane for a fluidization number of 6 and a measurement height of 36 cm. (For interpretation of the references to color in this figure legend, the reader is referred to the web version of this article.)

A detailed procedure to characterize bubbles on the basis of optical data is shown in Maurer (2015), Rüdüsüli et al. (2012a). Fig. 8 shows an excerpt of a binary signal (thin black line) which was acquired by placing the fictitious probe tip on a certain pixel of the reconstructed X-ray signal and scanning its value over time. Usually, optical measurements do not provide a binary signal for which reason a threshold must be defined to determine when the passage of a bubble starts and ends. The adjustment of a representative threshold for optical signals was investigated in the scope of Rüdüsüli et al. (2012a). However, the generated fictitious optical signal is binary since the selected threshold of 0.75 was already applied during the reconstruction of the X-ray images. Again, the value of one is assigned to the emulsion phase; the value of zero represents a bubble.

The excerpt shows several events of a signal rise back to the value of one for only a few time increments during a period of zero values. Hence, it might be assumed that this signal change shows two separate rising bubbles in a very short distance to each other. However, it should be considered that the measurement frequency is 250 Hz so one time increment only covers four milliseconds.

For comparable experimental conditions, a typical time gap between two bubbles that are detected by an optical sensor is in the range of one and two seconds which corresponds to bubble frequency of 30–60 bubbles per minute depending on the fluidization number and the measurement height (Rüdüsüli et al., 2012a). Hence, it seems very unlikely that two bubbles follow each other in a time period of only a few milliseconds without having coalesced before. It can therefore be assumed that a signal change from zero to one for a time period of only a few milliseconds belongs to the same bubble. This signal change may be caused by a locally higher particle concentration inside the bubble or due to artefacts that are generated in the bubble reconstruction process.

Sudden changes of the signal for a few time increments like they are shown in Fig. 8 have a great influence on the bubble properties determined with the optical evaluation. They interrupt the gapless time period  $t_b$  below the threshold and therefore lead to much shorter effective chord lengths. To obtain representative results, a filter has to be applied to smooth the misleading events for which the signal switches its value from zero to one for only a few time increments. The filter can be adjusted by the maximum number of consecutive time increments that can be smoothed for the case that the binary signal switches its value from zero to one. One time increment corresponds to a time period of  $1/250$  s. Subsequently, the maximum number of consecutive time increments that can be smoothed by the filter corresponds to the number in brackets e.g. filter (5) or filter (10). In Fig. 8, the thick yellow line (filter (5)) and thick green line (filter (10)) show the effect of a filter which is able to filter out sudden changes in the signal of up to

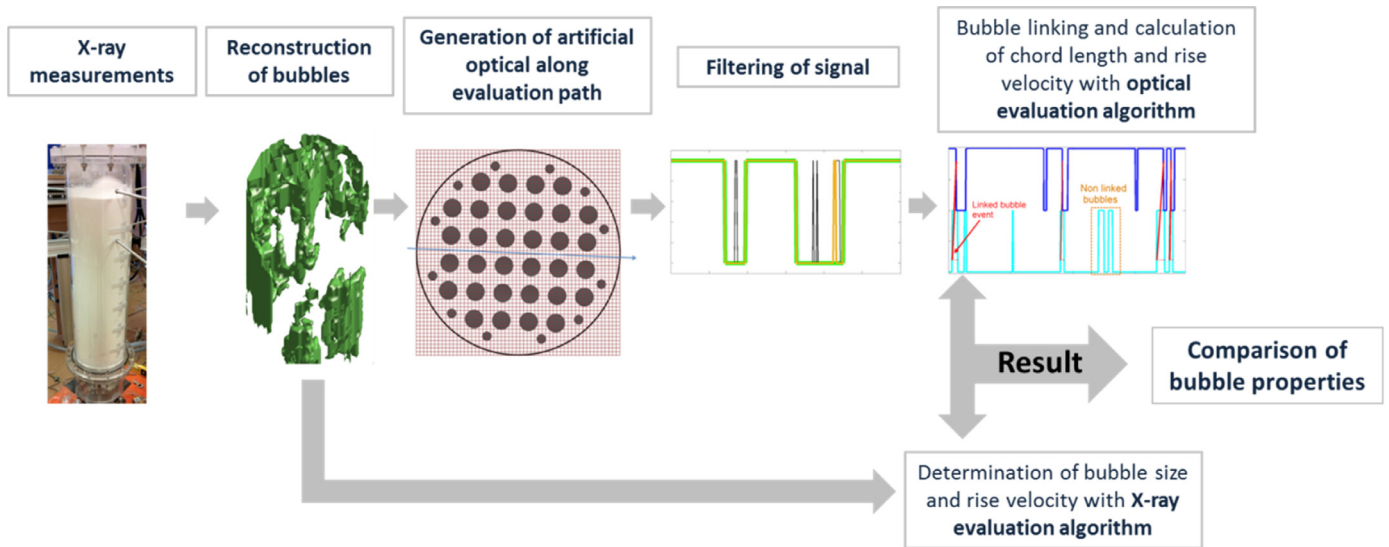


Fig. 9. Data processing scheme.

five or respectively ten increments of time. It should be mentioned that the maximum time gap that can be filtered out with filter (10) corresponds to 40 ms, hence, a too severe filtering is not expected.

A flow diagram that shows the single steps to generate an artificial optical signal out of the X-ray measurements is depicted in Fig. 9. The determined bubble properties by the optical and the X-ray evaluation algorithm can now be compared and possible deviations of the bubble properties be discussed.

## 5. Results and discussion

In this chapter, the artificial optical signal is used to determine the bubble rise velocity and the pierced chord length at each pixel along the evaluation path presented in Fig. 3(c). The obtained results are compared with available results from X-ray measurements in order to elaborate and find the reasons for the differences in the determined bubble properties by both measurement methods. The impact of filtering the fictitious optical data is evaluated and an annulus weighting of the bubble properties that are determined by the fictitious optical signal is introduced in order to obtain a statistically proper mean.

### 5.1. Influence of filter application on optical data evaluation

To link a bubble signal of the lower sensor to the corresponding signal of the upper sensor, the threshold exceedance at both sensors has to be within a defined number of time increments which depends on the measurement frequency, the vertical distance of the lower and upper optical sensor and the minimum detectable bubble rise velocity. A detailed description of the bubble linking algorithm is given in Rüdüsüli et al. (2012a). A representative excerpt of the binary artificial optical signal is shown in Fig. 10 in which some characteristic linkable and non-linkable bubble events are visible for a filtered signal.

As discussed in the previous section, single sudden changes of the signal have an influence on the bubble properties determined by the optical evaluation method. In the following, filters of different strengths are compared with the original, unfiltered signal to quantify the effect of the filter on the fraction and number of linked bubbles as well as its influence on the mean chord length and the mean bubble rise velocity. A description how the filter works is given in the previous section. The evaluation of each pixel

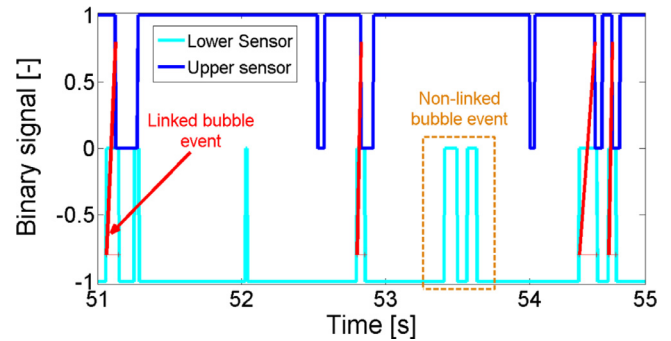


Fig. 10. Characteristics of bubble linking for a filtered signal.

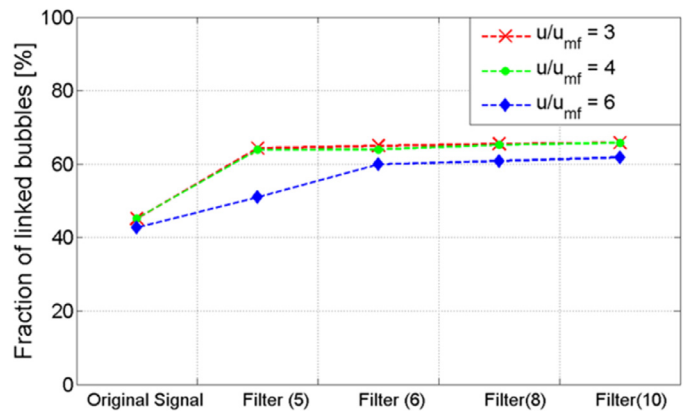


Fig. 11. Influence of filter strength on annulus weighted (see Section 5.2) fraction of linked bubbles for a measurement height of 56 cm.

along the centerline (see Fig. 3(c)) provides the data basis for the optical evaluation that is presented in the subsequent figures. The depicted points correspond to the mean value of all detected bubbles along the evaluation path.

The influence of the filter application on the fraction of linked bubbles is shown in Fig. 11. The fraction of linked bubbles is defined by the total number of linked bubbles divided by the amount of all threshold exceedances for the lower sensor. Hence, it decreases with an increasing number of sudden changes in the sig-

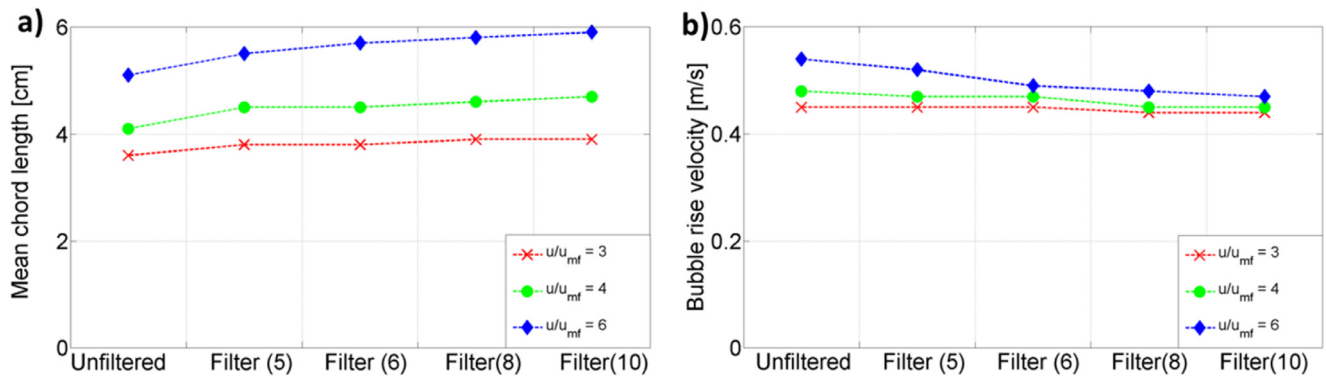


Fig. 12. Influence of filter application on mean chord length (a) and mean bubble rise velocity (b) for different fluidization numbers at a measurement height of 56 cm.

nal of the lower sensor. This is due to the fact that in most cases, sudden changes appear in only one of the two signals, since, for example, a bubble shows a temporarily and partially high fraction of dense material which is only detected by one of the two sensors. By the use of a filter that scans a minimum of six successive time increments which corresponds to a time span of 24 ms at a frequency of 250 Hz, a fraction of at least 60% linked bubbles is reached for all fluidization states.

The increase can be attributed to the fact that some sudden changes of the signal as they are shown in Fig. 8 are filtered out. Hydrodynamic investigations on a bubbling fluidized bed with vertical internals have shown that bubbles do not rise exactly in a vertical line (Schillinger et al., 2017). Due to bubbles rising with a lateral movement component, it may happen that the same bubble is not pierced by both the lower and the upper sensor. As a consequence of rising bubbles with a lateral displacement, the fraction of linked bubbles cannot reach 100%.

The influence of the filter strength on the mean chord length for a measurement height of 56 cm is shown in Fig. 12(a). As expected, the mean chord length rises with the application of a filter. If a filter is applied, the filter strength has a minor influence on the chord length except for the highest fluidization number. This could be explained by the fact that the signal duration of larger bubbles is in general longer for which reason also longer time periods with a signal rise from zero to one may occur. Hence, the longer sudden signal changes can only be flattened with a stronger filter.

Fig. 12(b) depicts the influence of the filter on the bubble rise velocity. It becomes apparent that the effect of the filter on the BRV at lower fluidization numbers is in general not as pronounced as it is the case for the chord length. This can be explained by the fact that in general, the time difference between the bubble detection at the lower and upper sensor which determines the BRV is not influenced by the filter. However, for a fluidization number of six, the application of a filter leads to a decrease of the BRV. This implies that filtering out “wrongly” linked bubbles decreases the determined bubble rise velocity since the bubble link of the filtered signal is switched to the next event resulting in a lower BRV.

## 5.2. Weighting of data generated by optical evaluation method based on annulus area

For local optical measurements, it should be noted that the result of a measurement position close to the center of the column has a much lower contribution to the overall mean value (due to the smaller area of the annulus that corresponds to the measurement position) compared to measurement positions that are close to the wall of the column (see Fig. 13). It is therefore necessary to

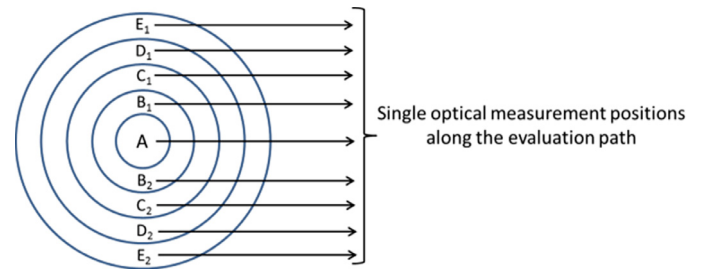
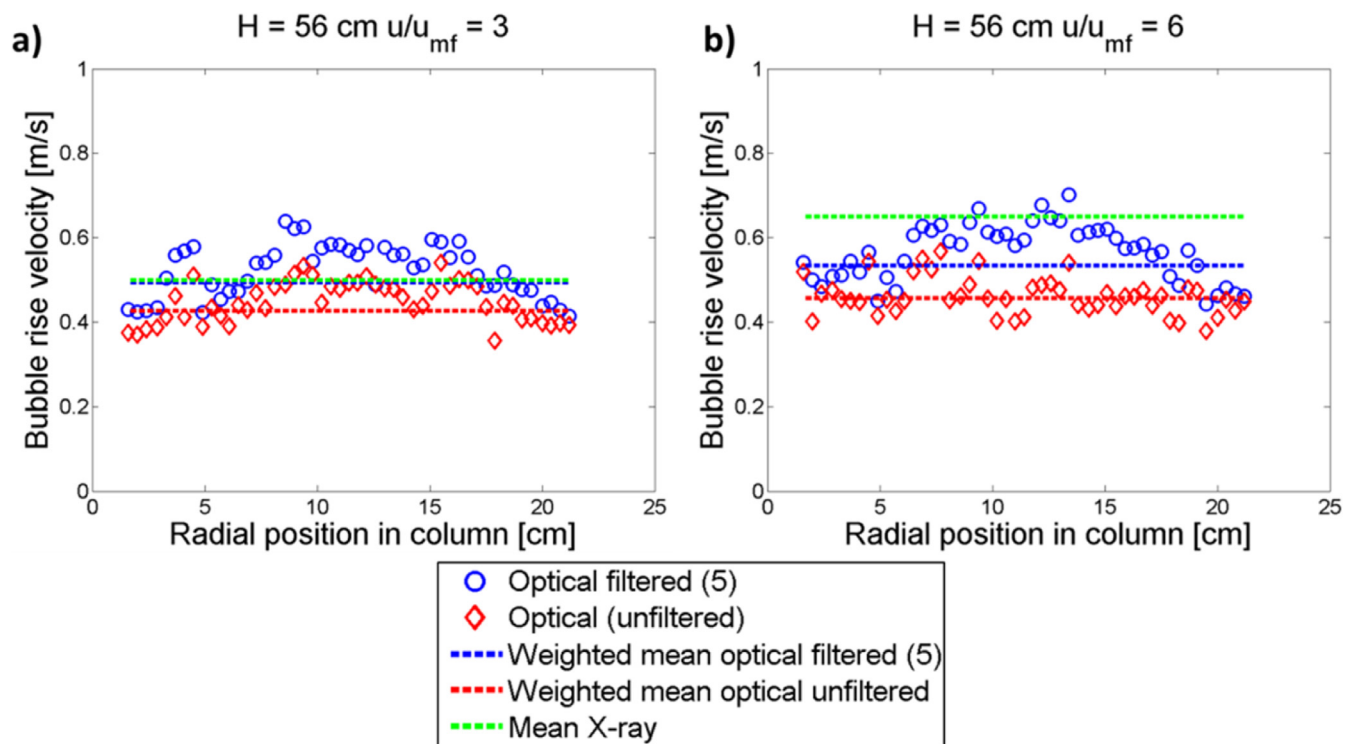


Fig. 13. Schematic principle to weight the single optical measurement position to a mean value.

weight the single measurement points to get a reasonable mean value for the entire cross-section.

The contribution of the determined mean bubble rise velocity of every single measurement point (represented by the blue circles in Fig. 14) to the mean weighted chord length of all measurement positions (dashed blue line in Fig. 14) depends on the ratio between the area of the annulus where the measurement position is located to the total cross-sectional area. Although the vertical internals disrupt the annulus uniformity, this method was selected to weight the single measurement points since it fills out the entire column. A weighting of the single measurement points by areas of rectangular rings could not completely cover the circular cross-section of the column. As a first approximation, it is assumed that the fraction of the area which is covered by internals is the same in each annulus. Larger deviations to this approximation apply to the innermost annuli. However, their contribution to the overall average is negligible due to the small area of the innermost circular rings.

Since there are always two measurement positions in one annulus, the average of both measurement positions is relevant for the calculation of the mean value over the entire cross-section. For example, to determine the contribution of the third innermost annulus in Fig. 13 to the mean value, the average of the measurement positions  $C_1$  and  $C_2$  is calculated and in the next step weighted by the area of annulus “C” relative to the total cross-section. The principle of the “annulus” weighting is applied in Sections 5.3 and 5.4 for the optical evaluation method to calculate the mean BRV and the mean chord length depicted in Figs. 14 and 18. For the investigated system with a resolution of  $55 \times 55$  pixels, the weighting is conducted over 27 circular rings. Unlike the data analysis with an artificial optical signal, the X-ray method directly provides bubble properties for the entire cross section of the bubbling fluidized bed for which reason an annulus weighting is inappropriate.



**Fig. 14.** Mean BRV from X-ray evaluation (solid line) and mean annulus weighted BRV from optical evaluation (dashed lines). Each radial measurement point matches with the mean BRV of the corresponding pixel on the evaluation path in Fig. 3(c). (For interpretation of the references to color in this figure legend, the reader is referred to the web version of this article.)

### 5.3. Comparison of bubble rise velocity between optical and X-ray evaluation method

If the shape of a bubble does not change between the lower and upper detector array, it is expected that both the X-ray evaluation method as well as the evaluation by means of the artificial optical signal result in the same bubble rise velocity. This hypothesis is based on the fact that the time difference  $\Delta t$  which is used to calculate the bubble rise velocity is the same, irrespective whether the beginning of the bubble (optical evaluation) or the center of gravity (X-ray evaluation) is taken as reference point (see Eq. (6)). However, it turned out that statistical effects have to be considered carefully if X-ray results are compared with results from optical measurements as it will be shown in this section.

For a measurement height of 56 cm and fluidization numbers of three and six, Fig. 14 shows the BRV calculated on basis of the filtered and unfiltered optical signal in dependence of the radial measurement positions along the evaluation path (see Fig. 3(c)). Furthermore, the mean annulus weighted BRV of the optical evaluation and the mean BRV of the X-ray evaluation are depicted. To obtain comparable results, the BRV which is based on the X-ray evaluation only includes the vertical velocity component since the fictitious optical sensor cannot detect the lateral velocity component of rising bubbles. For a fluidization number of three, the mean bubble rise velocity of the optical filtered signal almost corresponds to the mean bubble rise velocity determined by the X-ray evaluation. For a fluidization number of six, it is notable that the X-ray evaluation results in a higher mean BRV compared to the optical evaluation of the data. As mentioned above, a significant difference between the mean velocities determined by both methods was not expected for which reason the interpretation of the data is challenging.

An explanation for possible discrepancies could be the fact that bubbles of various sizes may have a different mean bubble rise ve-

locity depending on the fluidization number  $u/u_{mf}$  and the measurement height. Fig. 15(a) shows the number of bubbles classified by their volume equivalent bubble diameter ( $d_{b,vol,eq.}$ ) and their bubble rise velocity determined by the X-ray evaluation method for a measurement height of 56 cm and a fluidization number of three. Fig. 15(e) shows the mean horizontal cross-sectional area of the bubbles in the corresponding size interval of the volume equivalent diameter. The larger the bubbles are extended into the horizontal directions, the more likely they are pierced by an optical sensor. Fig. 15(g) shows the probability of a pierced bubble to lie within a certain interval of the volume equivalent diameter. The probability is calculated as the product of the mean cross-section and the number of bubbles in the corresponding size interval of the volume equivalent diameter divided by the absolute number of detected bubbles.

For a measurement height of 56 cm and a fluidization number of three, the BRV determined by the optical evaluation method almost corresponds to the BRV determined by the X-ray evaluation method as presented in Fig. 14(a) since the mean BRV (see Fig. 15(c)) in the size intervals with a high piercing probability (see Fig. 15(g)) does not vary to a large extent.

However, for a measurement height of 56 cm and a fluidization number of six, the optical evaluation resulted in a lower BRV compared to the X-ray evaluation (see Fig. 14(b)). This finding can not only be explained by the results shown in Fig. 15(b) and (d) since the number based mean BRV in each interval is not significantly below the number based mean BRV of all bubbles. Hence the question arises how the optical measurement method can result in a lower bubble rise velocity compared to the X-ray method? In order to find an explanation, the relation between the probability to pierce a bubble in a certain size interval and the corresponding bubble rise velocity has to be investigated.

Since the larger bubbles are more likely to be pierced by an optical sensor (see Fig. 15(h)), the lower mean BRV of bubbles with

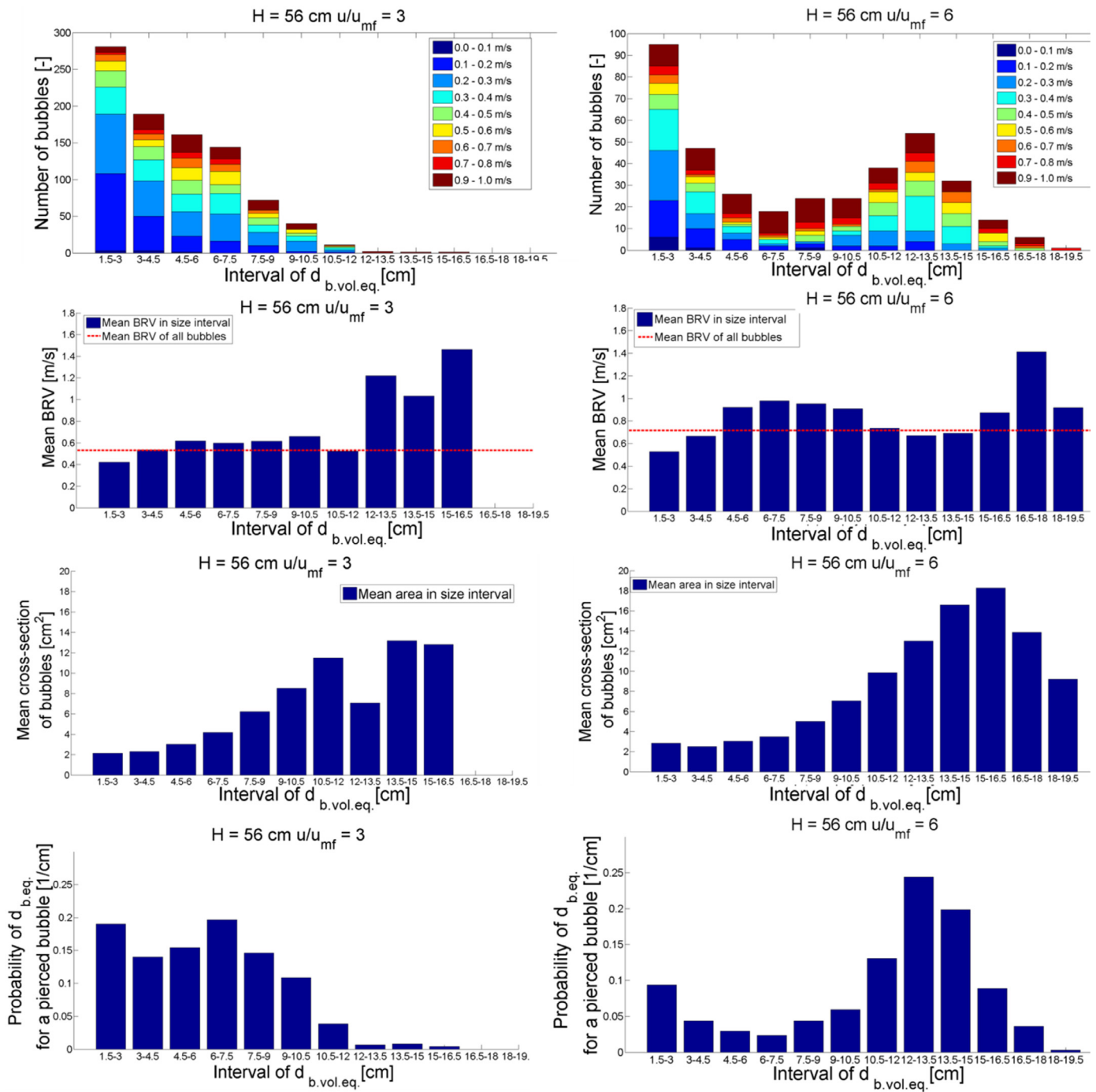


Fig. 15. Classification of the number of bubbles by their volume equivalent diameter and their velocity (color) based on the X-ray evaluation method at a height of 56 cm for fluidization numbers of three and six.

a larger size shows a disproportionately high contribution to the mean BRV determined by the optical sensor. Hence, the optical evaluation may result in a lower mean BRV than the X-ray evaluation for a measurement height of 56 cm and a fluidization number of six.

This discrepancy can be further explained by a scatter plot of the bubble rise velocity and the mean cross-section of each detected bubble shown in Fig. 16 for a fluidization number of six and a measurement height of 56 cm. The cross-section is defined by a horizontal cut through the bubbles. The bubbles with a high BRV tend to have a lower cross-sectional area and therefore a lower probability to be pierced. Inversely, bubbles with a

large cross-sectional area (high piercing probability) tend to show a lower BRV. Hence, it can be explained why the optical measurement method leads to a lower number based mean bubble rise velocity compared to the X-ray evaluation method (see Fig. 14(b)). The trend towards lower bubble rise velocities for bubbles with a larger horizontal cross-sectional area could be explained by their increased flow resistance compared to slender bubbles that have to push aside less bed material while ascending.

For future measurement campaigns that are based only on local optical measurements, it should be considered for which settings the determined bubble rise velocity has to be corrected. As a general trend towards higher fluidization numbers, it turned out

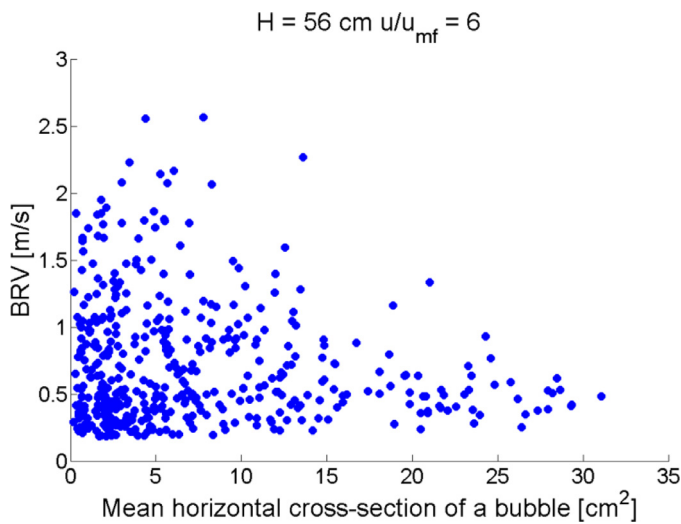


Fig. 16. Scatter plot of BRV and the corresponding mean cross-sectional area for all detected bubbles at a measurement height of 56 cm and a fluidization number of six.

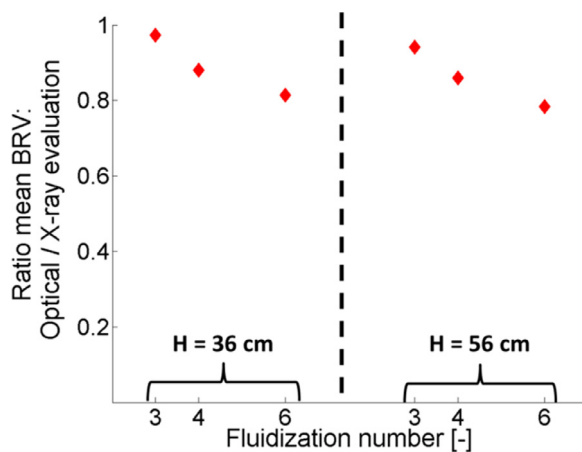


Fig. 17. Ratio of bubble rise velocity determined by optical evaluation method to X-ray evaluation method for measurement heights of 36 cm and 56 cm and fluidization numbers of 3, 4 and 6.

that the bubble rise velocity determined by the optical evaluation is lower than the rise velocity of all bubbles that is measured by the X-ray evaluation as depicted in Fig. 17 which shows the ratio of the mean bubble rise velocity determined by both evaluation methods. This is most probably due to the fact that the number of slugs increases towards higher fluidization number with the consequence that the slugs which have a large cross-sectional area in the horizontal direction and at the same time a low bubble rise velocity are pierced more likely. Fig. 17 can be used as an assistance to correct the bubble rise velocity of future optical measurements in a column with vertical internals for similar configurations.

#### 5.4. Comparison of the bubble size between optical and X-ray evaluation method

Fig. 18 shows the chord length of the optical evaluation with and without application of a filter for all pixels along the evaluation path (see Fig. 3(c)) at a measurement height of 56 cm and fluidization numbers of four and six. It emerges that the chord length at any single pixel is smaller than the mean volume equivalent bubble size of the X-ray evaluation. In general, the annulus weighted chord length is up to 25% smaller than the mean volume

equivalent bubble size determined by the X-ray evaluation. At first glance, this finding seems not to be in accordance with the results that are presented in the study of Rüdüsüli et al. (2012b) which stated that the mean chord length almost corresponds to the mean bubble diameter for the case of spherical bubbles since the error of piercing larger bubbles is compensated by the fact that a bubble is often not pierced close to its volume equivalent diameter.

However, for the present study, there may be different explanations for this apparent discrepancy to the results presented in the scope of Rüdüsüli et al. (2012b). Due to the evaluation along the centerline as shown in Fig. 3(c), the same bubble is pierced at several radial positions by the fictitious optical probe as visualized schematically for a spherical bubble in Fig. 19. Therefore, the fictitious optical sensor does not pierce a lot of bubbles next to their volume equivalent diameter but rather apart from their centerline resulting in a lower mean chord length compared to the actual volume equivalent bubble diameter which is determined by the X-ray method. The statistical mean expectation value for the chord length of a randomly pierced bubble at various positions is 2/3 of the bubble diameter if the bubble has a perfectly round shape. This value is based on the ratio between the volume of a sphere to its projected area (Sjöstrand, 2003).

In Fig. 20, the determined chord length distribution for the artificial optical signal along the centerline of the column is compared with the distribution of the volume equivalent diameter over the entire cross-section at a measurement height of 56 cm for fluidization numbers of four and six. The volume equivalent diameter distribution for a fluidization number of six (see Fig. 20(b)) shows a second peak at a diameter between 10 and 17 cm, whereas, no second peak is detectable for the same distribution at a fluidization number of four as depicted in Fig. 20(a). For both fluidization numbers, the chord length distribution decreases monotonically towards larger sizes.

The different shape of the chord length distribution and the bubble volume equivalent diameter distribution for a fluidization number of six (see Fig. 20(b)) can be explained due to the formation of slugs which are visible in Fig. 21(b). The presented bubble images are a quasi-3-dimensional reconstruction of the fluidization state since the vertical axis corresponds to the time. Bubbles rising with the mean bubble rise velocity are neither elongated nor shrunken in this illustration. However, bubbles that are slower than the mean rise velocity appear as apparently elongated in the vertical direction in the graphical presentation of the fluidization state depicted in Fig. 21, although, their actual shape is much flatter. An apparent elongation especially applies to slugs since they are slower than the mean bubble rise velocity (see Fig. 15(b) and (d)) for which reason some bubbles presented in Fig. 21(b) seem to be elongated in the vertical direction.

A slug that covers the majority of the cross-section exhibits a high volume that is determined with the X-ray evaluation, and therefore results in a large volume equivalent diameter. Conversely, piercing a slug that is shrunk in the vertical direction with the fictitious optical sensor does not necessarily lead to a large chord length, for which reason there is no second peak in the chord length distribution. For a fluidization number of three, the bubbles are significantly smaller as depicted in Fig. 21(a). Hence, no further peak for bubbles with a size between 13 and 19 cm is present for the volume equivalent diameter distribution. For the reasons mentioned above, great caution should be exercised in drawing conclusions on bubble properties if the bubble size is determined with different measurement respectively evaluation methods. Hence, statistical methods like a Monte Carlo (MC) simulation could be an option to reveal the reasons for the discrepancy in the bubble properties derived by the optical and the X-ray evaluation method.

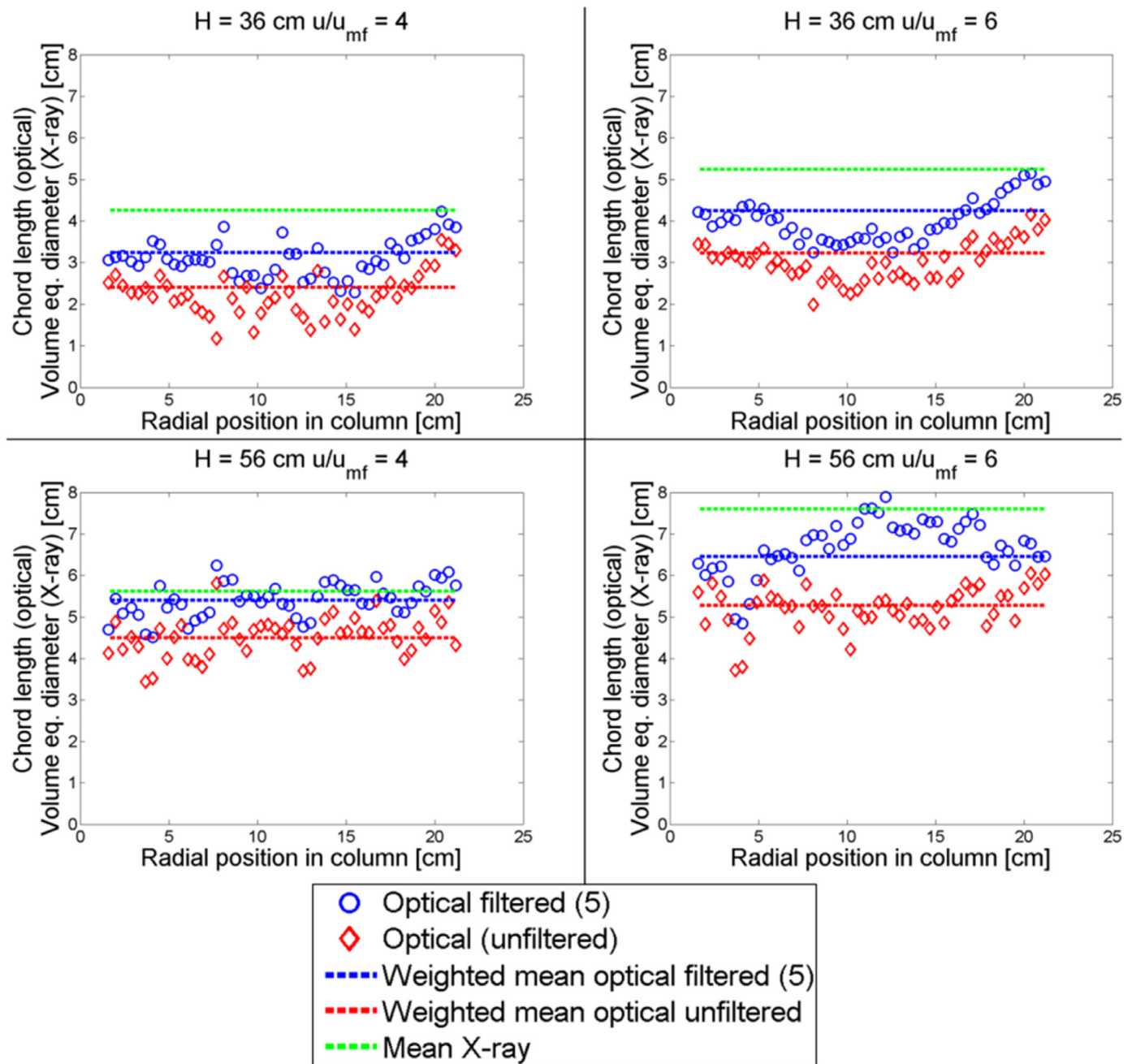


**Fig. 18.** Mean bubble size from X-ray evaluation (green dashed line) and mean annulus weighted chord lengths from optical evaluation (red and blue dashed lines). Each radial measurement point matches with the mean chord length of the corresponding pixel on the evaluation path in Fig. 3(c). (For interpretation of the references to color in this figure legend, the reader is referred to the web version of this article.)

## 6. Monte Carlo simulation

In this section, the results of a Monte Carlo (MC) simulation are presented in order to investigate the question: “Which chord length distribution does a perfectly working local optical sensor determine compared to the volume equivalent diameter of all bubbles in the column?” Moreover, the MC-simulation is used to identify the reasons for the gap between the bubble properties derived by the optical and the X-ray evaluation method. The procedure and the results of the MC-simulation are described in the following sections.

Rising bubbles in a fluidized bed are simulated with the aim to generate an undisturbed signal of an artificial local optical sensor. This signal is used to determine the bubble properties with

the standard algorithm to evaluate an optical signal (Rüdisüli et al., 2012a). The derived bubble properties are compared to the properties of all bubbles that were generated in the Monte Carlo simulation.

### 6.1. Principle and procedure of the Monte Carlo simulation

Fig. 22 shows the schematic procedure of the conducted Monte Carlo simulation. In the first step, a logarithmic normal distribution is fitted both on the bubble rise velocity and the volume equivalent bubble diameter distribution of the bubbles that were determined by X-ray measurements in the scope of Maurer (2015). The distributions were fitted for all six combinations between the measurement heights of 36 and 56 cm and the fluidization numbers of 3,

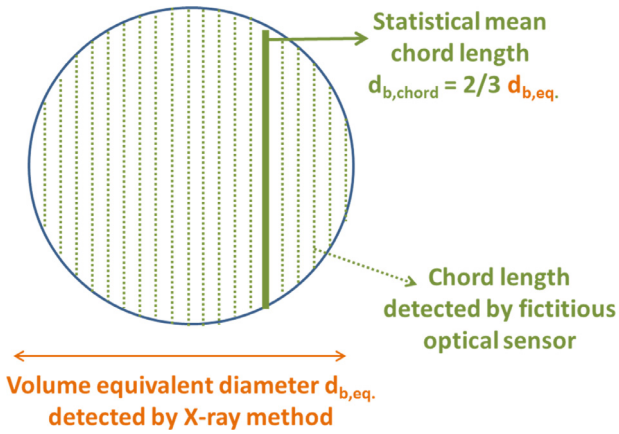


Fig. 19. Visualization of mean chord length for a bubble pierced at various positions by the fictitious optical sensor and the volume equivalent bubble diameter (X-ray method).

4 and 6. Hence, each run of the Monte Carlo simulation was conducted separately based on the corresponding random parameters for the simulated measurement height and fluidization number.

In a bubbling fluidized bed with vertical internals, the bubbles may be restricted in their shape due to the presence of internals in the column. This leads to a broad spectrum for the shape of the bubbles as pointed out in Maurer et al. (2015b), Schillinger et al. (2017). An exemplary excerpt of the reconstructed bubbles is depicted in Fig. 23 which shows that the bubble shape can be manifold. Hence, in the scope of the Monte Carlo simulation, the geometry of the bubbles has to be approximated by a shape that may cover the broad range of possible shapes that are present in a real bubbling fluidized bed. Ellipsoidal bubbles were chosen since their geometry can be described mathematically and their shape is most likely representing bubbles in a fluidized bed with vertical internals. The bubble ellipsoids were defined by the diameter  $d_1$  in both horizontal directions of the simulated column and the independent diameter  $d_2$  into the vertical direction of the column. Due to the independent determination of the random numbers for the vertical and horizontal diameters of the bubble, the ellipsoidal bubble shape may be pronounced to a greater or lesser extent. Next to the simulation of ellipsoidal bubbles, a sepa-

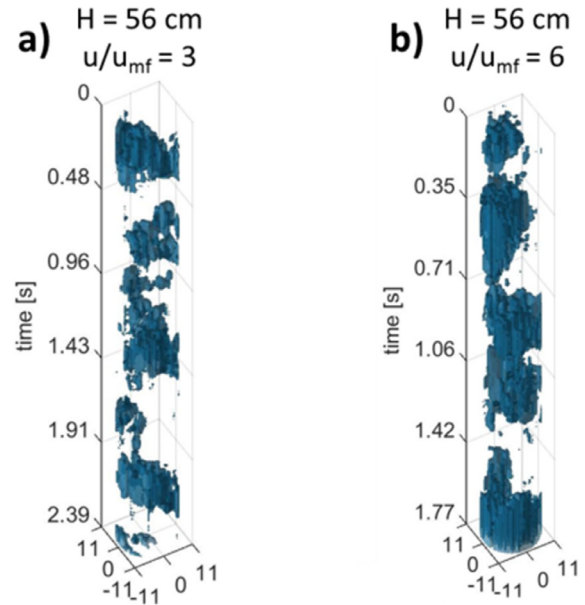


Fig. 21. Reconstructed bubbles at H=56cm for fluidization numbers of 3 and 6 based on X-ray measurements.

rate Monte Carlo simulation was conducted for perfectly spherical bubbles which should represent the theoretical case.

In total, the rise of 5000 individual bubbles with a frequency of 10 bubbles per second was simulated for each setting. The starting point of a bubble was selected randomly across the cross-section of the column. After a bubble is generated at the bottom of the simulated column, the velocity and the size of this bubble stayed constant along the height of the column. The simulated column has a diameter of 22 cm and a resolution of 5 pixels per cm in all dimensions.

The volume of a rising bubble in the simulation is described by the value of one, whereas, the cells where no bubble is located have the value of zero. The fictitious sensor samples the value of the cell that is located in the center of the column at heights of 15 and 16 cm. If a bubble reaches the cells where the sampling takes place, the value of this cell changes from zero to one as long as the bubble is present in the corresponding cell.

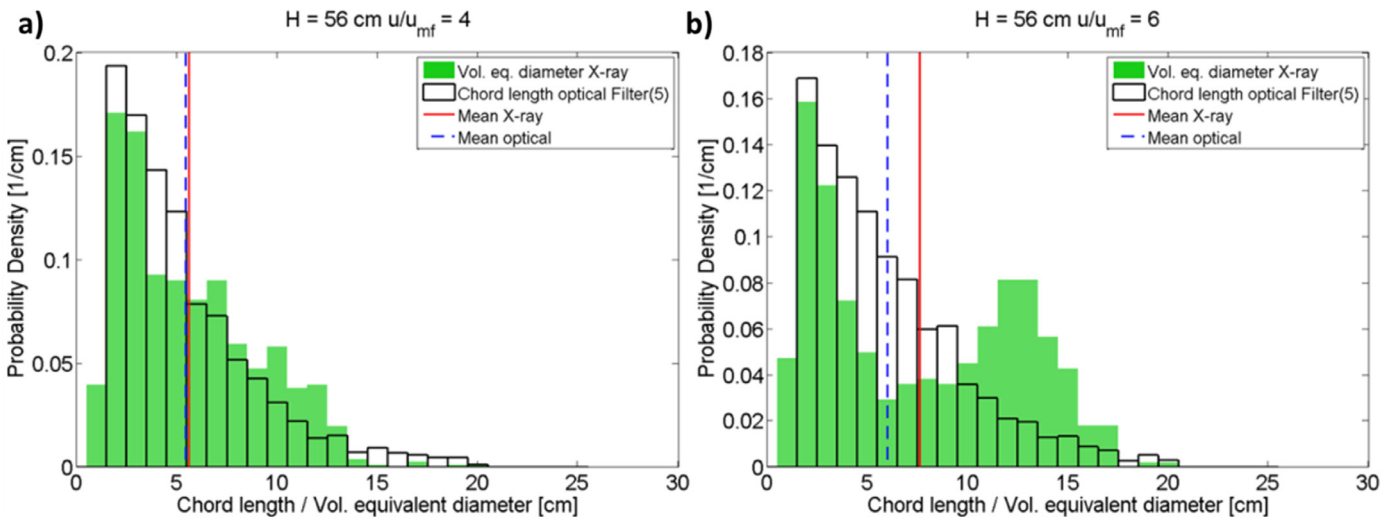


Fig. 20. Histograms of the chord length distribution for the filtered artificial optical signal and the volume equivalent diameter (above the entire cross-section) for the X-ray evaluation at H = 56 cm and  $u/u_{mf}$  = 4 and 6.

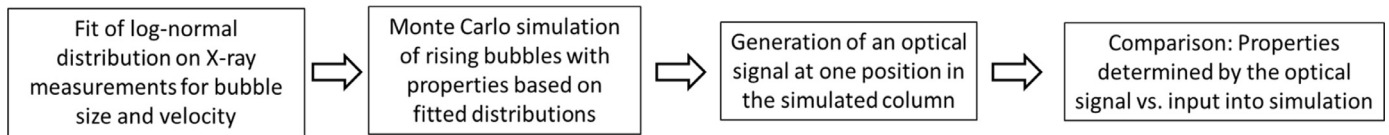


Fig. 22. Schematic procedure of the Monte Carlo simulation.

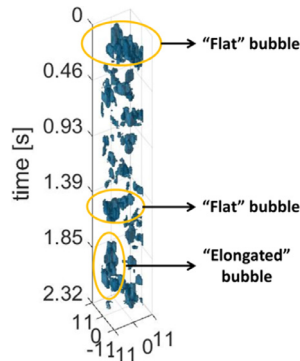


Fig. 23. Quasi 3-dimensional reconstruction of the bubble shape for a fluidization number of 3 at a measurement height of 36 cm by means of X-ray measurements. The vertical internals are not visualized. Picture adapted from (Maurer, 2015).

In the next step, the chord length and the bubble rise velocity are determined by means of the optical evaluation algorithm. These properties can now be compared to the properties of all bubbles that were generated in the scope of the simulation.

### 6.2. Results of MC-simulation for spherical bubbles

For spherical bubbles, Fig. 24 shows the bubble size and the bubble rise velocity distribution of all simulated bubbles (input) compared to the distributions determined by the optical evaluation. The results for the spherical bubbles are in good accordance with the work of Rüdüsüli et al. (2012b) who stated that the mean chord length determined by an optical sensor roughly corresponds to the mean diameter of the underlying bubble size distribution. This is due to the fact that a local optical sensor pierces more likely larger bubbles compared to smaller bubbles, whereas, the bubbles are often not pierced with a chord length that is close to the diameter. However, the work of Rüdüsüli et al. has focused on the simulation of smaller bubbles for which reason there might be slight deviations to the present work. As expected, the BRV distribution determined by the optical evaluation corresponds almost exactly to the BRV distribution of all simulated bubbles.

### 6.3. Results of MC-simulation for ellipsoidal bubbles

For bubbles with an ellipsoidal geometry, Fig. 25(a) presents the distribution of the volume equivalent diameter for all simulated bubbles compared to the chord length distribution determined by the local optical measurement. In contrast to the simulation of spherical bubbles, it turns out that the chord length distribution is shifted towards a smaller size compared to the volume equivalent diameter distribution of all simulated bubbles. This results in a mean chord length which is roughly 25% smaller than the mean input diameter of all bubbles.

The emerging gap between the mean chord length and the mean volume equivalent bubble diameter may be explained by the ellipsoidal bubble geometry. If the bubble diameter  $d_1$  in the horizontal direction is larger than the diameter  $d_2$  in the vertical direction, the pierced chord length of an ellipsoidal shaped bubble is smaller than the volume equivalent diameter of the corre-

Table 1

Factor X to correct the mean chord length for ellipsoidal shaped bubbles.

Height [cm]	36	36	36	56	56	56
$u/u_{mf}$ [-]	3	4	6	3	4	6
$X = \frac{d_{chord, optical}}{d_{vol, eq, input}}$	0.73	0.7	0.71	0.73	0.77	0.74

sponding bubble. On the other hand, if an ellipsoid is elongated in the z-direction, the chord length may be larger than the volume equivalent diameter. However, bubbles of a certain volume V that are elongated in the horizontal direction are more likely to be pierced than bubbles of the same volume V that are elongated in the vertical direction. The different piercing probabilities of horizontally and vertically elongated bubbles explain the gap between the mean chord length of the optical evaluation to the mean volume equivalent diameter that are both marked in Fig. 25(a).

Fig. 25(b) shows the bubble rise velocity distribution for the input and the optical evaluation. As expected, the bubble rise velocity distribution that is determined by the optical sensor is almost identical to the BRV distribution of all simulated bubbles.

Based on the results of the Monte Carlo simulation, a factor X is defined that describes the ratio between the mean chord length determined by an optical sensor and the mean volume equivalent diameter of all bubbles with an ellipsoidal geometry. The determined factors are given in Table 1 for all investigated settings. This factor may now be applied to correct the chord length which is generated by the fictitious optical signal based on the X-ray measurements (see Fig. 18) as well as the chord length of upcoming optical measurements under the assumption that the bubbles can be regarded as ellipsoids in a first approximation.

### 6.4. Correction of the mean chord length

In this section, the results of the Monte Carlo simulation are applied to correct the mean chord length that is calculated based on a fictitious optical signal which generated on the basis of X-ray measurements. The uncorrected mean chord lengths have already been presented in Section 5.4. Fig. 26 depicts the mean corrected chord length based on the factors shown in Table 1 for each measurement position along the evaluation path and the mean volume equivalent bubble diameter determined by the X-ray evaluation. For a measurement height of 36 cm, the gap between the mean bubble sizes which are determined by both evaluation methods could be reduced significantly in comparison to the uncorrected chord lengths (see Fig. 18). For a measurement height of 56 cm, the mean chord length overestimates the mean volume equivalent bubble diameter by a maximum of 15–20%. However, with regard to the application of the factor, it should be mentioned that the correction factor is based on a Monte Carlo simulation of perfectly ellipsoidal shaped bubbles. This shape was selected since the geometry can be described mathematically and since this geometry can be regarded as a first approximation for the actual bubble shape in a fluidized bed with vertical internals. More specific correction factors could be derived by simulating a bubbling fluidized bed with vertical internals in the scope of computational fluid dynamic studies. Hence, a transfer of these findings to other bubble

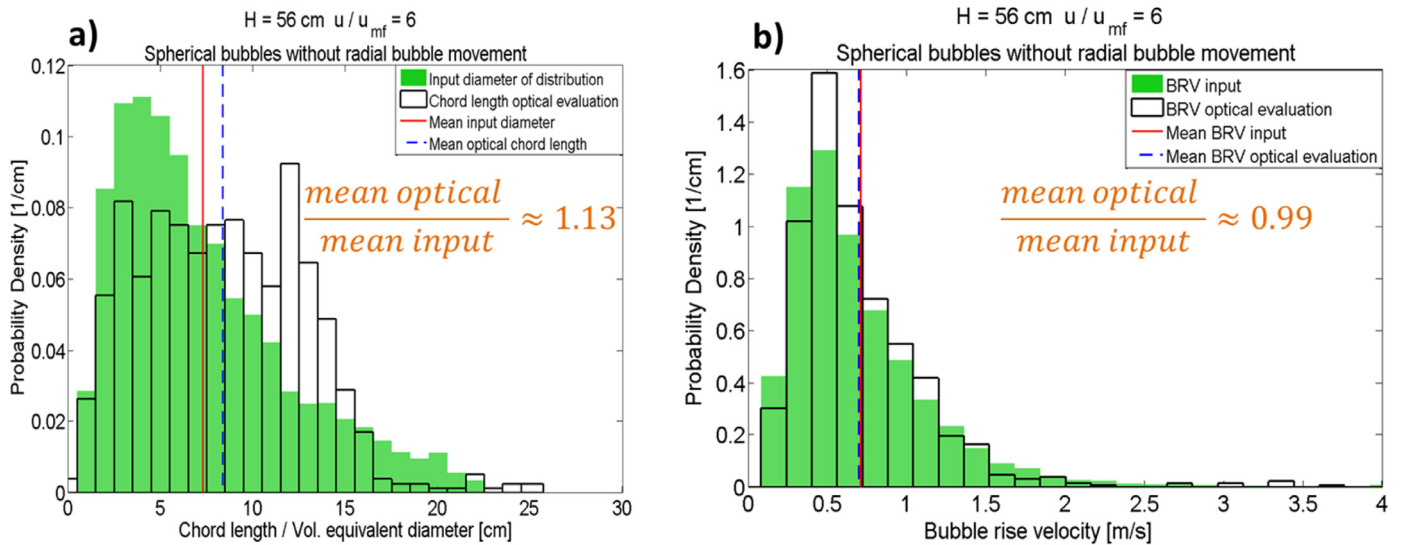


Fig. 24. Comparison of diameter (a) and bubble rise velocity (b) distribution for the input into the MC-simulation with the results generated by the optical evaluation for spherical bubbles.

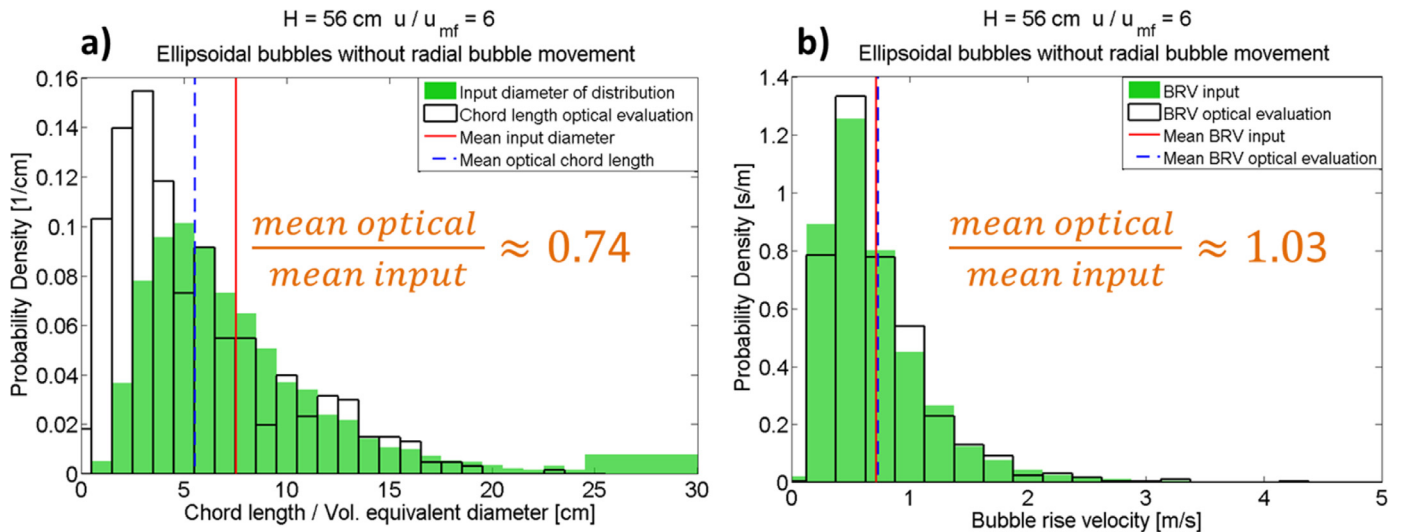


Fig. 25. Comparison of diameter vs. chord length (a) and bubble rise velocity (b) distribution for the input into the MC-simulation with the results generated by the optical evaluation for ellipsoidal bubbles.

shapes that may appear in a BFB with a different column design cannot be conducted without further investigations.

## 7. Conclusions

Optical measurements are commonly used to determine the hydrodynamics in different kinds of bubbling fluidized beds (van Ommen and Mudde, 2007). It could be shown that the bubble properties which are obtained by local optical measurements have to be considered cautiously due to statistical effects. This conclusion is not only limited to the geometry that was investigated in the scope of this study, but should be taken into account for the interpretation of any kind of data sets that are based on optical probes.

Explicit intention of this work was not to describe the hydrodynamic behavior of a bubbling fluidized bed as it is conducted in Maurer et al. (2015b,c) and Schillinger et al. (2017), but, to point out possible differences concerning the determined bubble properties between the evaluation method of an X-ray signal and an optical signal.

This investigation was conducted since in large scale fluidized bed reactors at hot and reactive conditions, it is not always possible to perform X-ray measurements that provide information of the fluidization state over the entire cross section. At PSI, an optical sensor was developed in order to enable hydrodynamic measurements in a bubbling fluidized bed reactor under these conditions. Optical probing is a comparatively easy method to examine the local state of fluidization. However, optical measurements have the drawback that only the chord length and not the volume equivalent diameter of the bubbles are accessible since this method is limited to a certain position in the column. Hence, evaluating the difference between both methods is inevitable to judge future measurements with a local optical sensor. To achieve a direct comparison between the results obtained by both evaluation methods, existing hydrodynamic X-ray measurements on a bubbling fluidized bed with vertical internals were for the first time used as source to generate an artificial optical signal at defined positions in the column.

Concerning the bubble rise velocity, it turned out that for larger fluidization numbers, the mean BRV that is determined by the op-

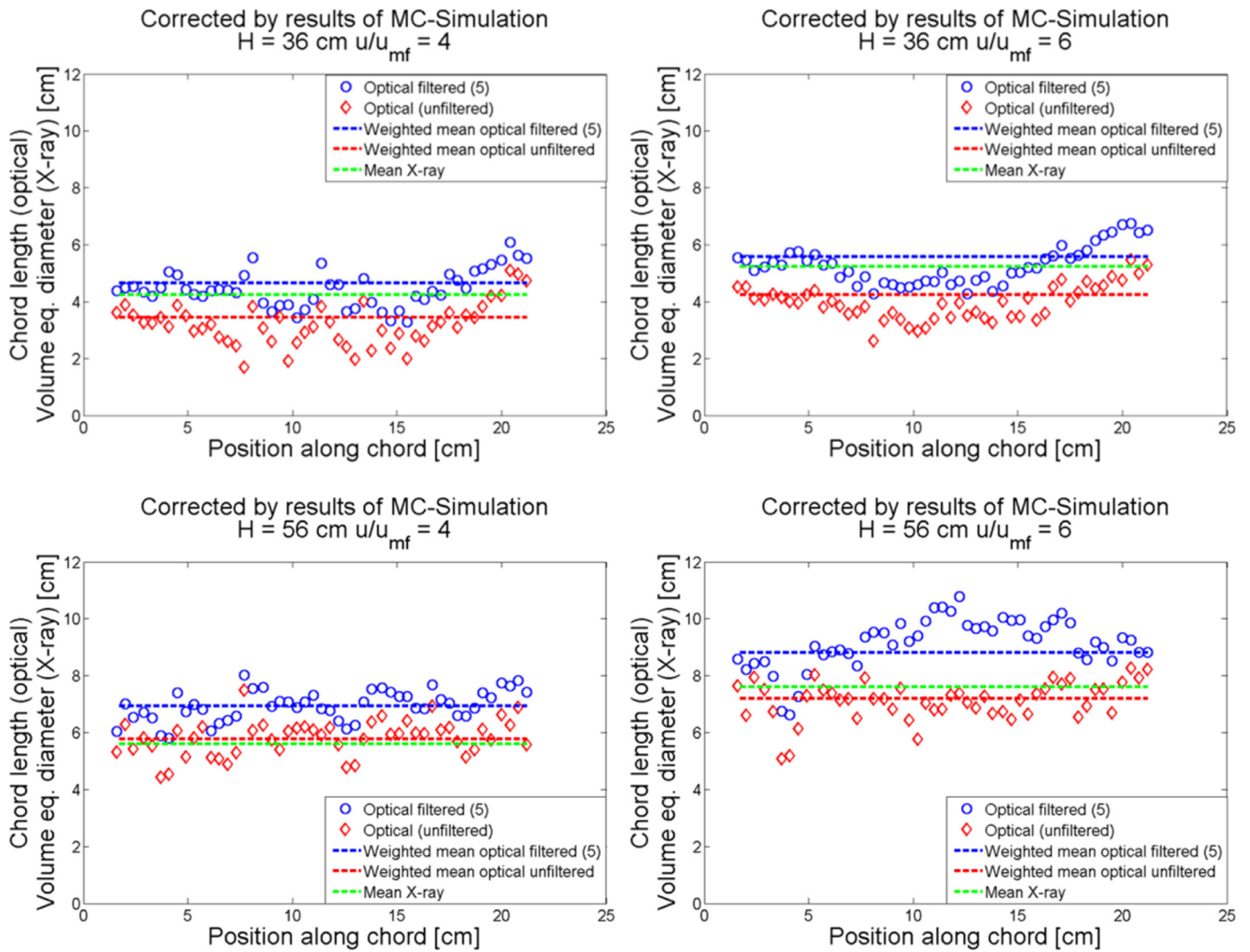


**Fig. 26.** Corrected mean chord lengths by results of MC simulation in comparison to bubble size determined by X-ray evaluation for  $H=56$  cm and fluidization numbers of 4 and 6.

tical evaluation method tends to be smaller than the BRV which is obtained by the X-ray evaluation method. This discrepancy could be explained by the fact that bubbles with a larger horizontal cross-sectional area show a tendency to rise with a slower mean BRV compared to bubbles with a smaller cross-sectional area. Hence, the higher probability to pierce these larger bubbles with an optical sensor reflects in the lower number based mean rise velocity that is determined by this method. The mean bubble rise velocity of future measurement campaigns with local, optical sensors can now be corrected by a factor (see Fig. 17) that describes the ratio between the mean BRV determined by local measurements to the mean BRV determined by measurements over the entire cross-section (X-ray). It should be pointed out that this factor is only valid in the scope of the investigated settings for beds with vertical internals concerning the fluidization numbers and measurement heights for which it can be applied to correct the bubble rise velocity at reactive conditions.

Several independent facts have to be considered in order to explain the finding that the mean chord length resulting from the optical evaluation is smaller than the mean volume equivalent diameter resulting from the X-ray evaluation. The analysis of the fluidization state by the fictitious optical probe along the entire diameter of the column has the effect that the same bubble may be pierced at several radial positions. For the case of spherical

bubbles, this leads to a mean chord length which is smaller than the mean volume equivalent diameter determined by the X-ray method. In case of a sufficiently high fluidization number, the formation of slugs that cover the entire cross-section may be a further reason why the mean chord length is smaller than the mean volume equivalent diameter. This is due to the fact that the pierced chord length of a slug is often significantly smaller than the corresponding volume equivalent diameter.

In order to investigate the relation between the mean chord length which is determined by a locally limited optical sensor and the mean bubble size of all simulated bubbles, a Monte Carlo simulation of rising bubbles was conducted. The simulation was performed both for bubbles with a spherical and an ellipsoidal geometry since the bubble shape in a fluidized bed with vertical internals can be regarded as ellipsoidal as a first approximation. It turned out that the mean chord length that is determined by the optical evaluation in the MC-simulation is in general smaller than the mean volume equivalent diameter of all simulated bubbles with an ellipsoidal shape. Based on these results, a factor was introduced which describes the ratio between the mean chord length of the optical evaluation and the mean volume equivalent diameter of all bubbles for the case of an ideal ellipsoidal geometry. The mean chord length increases if the factor is applied to the results of the optical measurements. For the most settings, the relative

deviation between both values could be reduced, although, after application of the factor, the mean chord length slightly overestimates the mean volume equivalent bubble diameter. Hence, correcting the mean chord length determined in future optical measurement campaigns by the factors presented in Table 1 is useful in terms of reducing the maximum error of local measurements.

In general, the knowledge obtained within the scope of this study allows a judgement and correction of the bubble properties resulting from future measurement campaigns at bubbling fluidized bed reactors under hot and pressurized conditions for which only optical probes will be available.

## Acknowledgment

This research project is financially supported by the Swiss Innovation Agency Innosuisse and is part of the Swiss Competence Center for Energy Research SCCER BIOSWEET. Further, support by the Energy System Integration platform (ESI) is gratefully acknowledged.

## References

- Acosta-Iborra, A., Sobrino, C., Hernández-Jiménez, F., de Vega, M., 2011. Experimental and computational study on the bubble behavior in a 3-D fluidized bed. *Chem. Eng. Sci.* 66, 3499–3512. doi:10.1016/j.ces.2011.04.009.
- Andersen, A.H., Kak, A.C., 1984. Simultaneous Algebraic Reconstruction Technique (SART): a superior implementation of the art algorithm. *Ultrasound Imaging* 6, 81–94. doi:10.1177/016173468400600107.
- Asegehegn, T.W., Schreiber, M., Krantz, H.J., 2011. Investigation of bubble behavior in fluidized beds with and without immersed horizontal tubes using a digital image analysis technique. *Powder Technol.* 210, 248–260. doi:10.1016/j.powtec.2011.03.025.
- Bai, W., Deen, N.G., Kuipers, J.A.M., 2010. Bubble properties of heterogeneous bubbly flows in a square bubble column. In: *Proceedings of the Sixth International Symposium on Multiphase Flow, Heat Mass Transfer and Energy Conversion*, pp. 563–568.
- Bakshi, A., Altantzis, C., Bates, R.B., Ghoniem, A.F., 2016. Multiphase-flow Statistics using 3D Detection and Tracking Algorithm (MS3DATA): methodology and application to large-scale fluidized beds. *Chem. Eng. J.* 293, 355–364. doi:10.1016/j.ces.2016.02.058.
- Clark, N.N., Turton, R., 1988. Chord length distributions related to bubble size distributions in multiphase flows. *Int. J. Multiph. Flow* 14, 413–424. doi:10.1016/0301-9322(88)90019-5.
- Davidson, J.F., Harrison, D., 1966. The behaviour of a continuously bubbling fluidized bed. *Chem. Eng. Sci.* 21, 731–738. doi:10.1016/0009-2509(66)87001-X.
- Glicksman, L.R., Lord, W.K., Sakagami, M., 1987. Bubble properties in large-particle fluidized beds. *Chem. Eng. Sci.* 42, 479–491. doi:10.1016/0009-2509(87)80010-6.
- Gogolek, P.E.G., Grace, J.R., 1995. Fundamental hydrodynamics related to pressurized fluidized bed combustion. *Prog. Energy Combust. Sci.* 21, 419–451. doi:10.1016/0360-1285(95)00010-0.
- Gomez-Hernandez, J., van Ommen, R., Mudde, R.F., Wagner, E., 2016. "Pressure and X-ray tomography characterization of the fluidization behavior of TiO<sub>2</sub> nanoparticles. In: *Proceedings of the Fluidization XV*.
- Grace, J.R., Clift, R., 1974. On the two-phase theory of fluidization. *Chem. Eng. Sci.* 29, 327–334. doi:10.1016/0009-2509(74)80039-4.
- Hillgardt, K., Werther, J., 1985. Lokaler Blasengas-Holdup und Expansionsverhalten von Gas/feststoff-wirbelschichten. *Chemie Ing. Tech.* 57, 622–623. doi:10.1002/cite.330570713.
- Liu, M., Zhang, Y., Bi, H., Grace, J.R., Zhu, Y., 2010. Non-intrusive determination of bubble size in a gas-solid fluidized bed: An evaluation. *Chem. Eng. Sci.* 65, 3485–3493. doi:10.1016/j.ces.2010.02.049.
- Maurer, S., 2015. Hydrodynamic characterization and scale-up of bubbling fluidized beds for catalytic conversion. ETH Zürich, Diss., ETH Zürich, Nr. 22722, Eidgenössische Technische Hochschule. doi:10.3929/ethz-a-010453120.
- Maurer, S., Gschwend, D., Wagner, E.C., Schildhauer, T.J., van Ommen, J.R., Biollaz, S.M.A., Mudde, R.F., 2016. Correlating bubble size and velocity distribution in bubbling fluidized bed based on X-ray tomography. *Chem. Eng. J.* doi:10.1016/j.ces.2016.02.012.
- Maurer, S., Schildhauer, T.J., van Ommen, J.R., Biollaz, S.M.A., Wokaun, A., 2014. Scale-up of fluidized beds with vertical internals: Studying the sectoral approach by means of optical probes. *Chem. Eng. J.* 252, 131–140. doi:10.1016/j.ces.2014.04.083.
- Maurer, S., Wagner, E.C., Schildhauer, T.J., van Ommen, J.R., Biollaz, S.M.A., Mudde, R.F., 2015a. X-ray measurements on the influence of optical probes on gas-solid fluidized beds. *Int. J. Multiph. Flow* 74, 143–147.
- Maurer, S., Wagner, E.C., Schildhauer, T.J., van Ommen, J.R., Biollaz, S.M.A., Mudde, R.F., 2015b. X-ray measurements of bubble hold-up in fluidized beds with and without vertical internals. *Int. J. Multiph. Flow* 74, 118–124. doi:10.1016/j.ijmultiphaseflow.2015.03.009.
- Maurer, S., Wagner, E.C., van Ommen, J.R., Schildhauer, T.J., Teske, S.L., Biollaz, S.M.A., Wokaun, A., Mudde, R.F., 2015c. Influence of vertical internals on a bubbling fluidized bed characterized by X-ray tomography. *Int. J. Multiph. Flow* 75, 237–249. doi:10.1016/j.ijmultiphaseflow.2015.06.001.
- Mudde, R.F., 2011. Bubbles in a fluidized bed: a fast X-ray scanner. *AIChE J.* 57, 2684–2690. doi:10.1002/aic.12469.
- Mudde, R.F., 2010. Time-resolved X-ray tomography of a fluidized bed. *Powder Technol.* 199, 55–59. doi:10.1016/j.powtec.2009.04.021.
- Mudde, R.F., Bruneau, P.R.P., van der Hagen, T., 2005. Time-resolved gamma-densitometry imaging within fluidized beds. *Ind. Eng. Chem. Res.* 44, 6181–6187. doi:10.1021/ie049091p.
- Rautenbach, C., Mudde, R.F., Yang, X., Melaaen, M.C., Halvorsen, B.M., 2013. A comparative study between electrical capacitance tomography and time-resolved X-ray tomography. *Flow Meas. Instrum.* 30, 34–44. doi:10.1016/j.flowmeasinst.2012.11.005.
- Rüdisüli, M., 2012. Characterization of rising gas bubbles in fluidized beds by means of statistical tools. *ETH/PSI*. doi:10.3929/ethz-a-007089625.
- Rüdisüli, M., Schildhauer, T.J., Biollaz, S.M.A., Ruud van Ommen, J., 2012a. Bubble characterization in a fluidized bed by means of optical probes. *Int. J. Multiph. Flow* 41, 56–67. doi:10.1016/j.ijmultiphaseflow.2012.01.001.
- Rüdisüli, M., Schildhauer, T.J., Biollaz, S.M.A., van Ommen, J.R., 2012b. Monte Carlo simulation of the bubble size distribution in a fluidized bed with intrusive probes. *Int. J. Multiph. Flow* 44, 1–14. doi:10.1016/j.ijmultiphaseflow.2012.03.009.
- Santana, D., Macias-Machin, A., 2000. Local bubble-size distribution in fluidized beds. *AIChE J.* 46, 1340–1347. doi:10.1002/aic.690460708.
- Schillinger, F., Maurer, S., Wagner, E.C., van Ommen, J.R., Mudde, R.F., Schildhauer, T.J., 2017. Influence of vertical heat exchanger tubes, their arrangement and the column diameter on the hydrodynamics in a gas-solid bubbling fluidized bed. *Int. J. Multiph. Flow*. doi:10.1016/j.ijmultiphaseflow.2017.07.013.
- Sjöstrand, N.G., 2003. On the average chord length. *VTT Symp. (Valtion Tek. Tutkimuskeskus)* 30, 7–9. doi:10.1016/j.aucene.2004.04.007.
- Sobrino, C., Acosta-Iborra, A., Izquierdo-Barrientos, M.A., de Vega, M., 2015. Three-dimensional two-fluid modeling of a cylindrical fluidized bed and validation of the Maximum Entropy method to determine bubble properties. *Chem. Eng. J.* 262, 628–639. doi:10.1016/j.ces.2014.10.014.
- Tebianian, S., Dubrawski, K., Ellis, N., Cocco, R.A., Hays, R., Reddy Karri, S.B., Leadbeater, T.W., Parker, D.J., Chaouki, J., Jafari, R., Garcia-Trinanes, P., Seville, J.P.K., Grace, J.R., 2016. Comparison of particle velocity measurement techniques in a fluidized bed operating in the square-nosed slugging flow regime. *Powder Technol.* 296, 45–52. doi:10.1016/j.powtec.2015.08.040.
- Tebianian, S., Ellis, N., Lettieri, P., Grace, J.R., 2015. X-ray imaging for flow characterization and investigation of invasive probe interference in travelling fluidized bed. *Chem. Eng. Res. Des.* 104, 191–202. doi:10.1016/j.cherd.2015.08.006.
- van Ommen, J.R., Mudde, R.F., 2007. Measuring the gas-solids distribution in fluidized beds – a review. In: *Proceedings of the Twelfth International Conference on Fluidization – New Horizons in Fluidization Engineering*.
- Verma, V., Li, T., Dietiker, J.-F., Rogers, W.A., 2016. Hydrodynamics of gas-solids flow in a bubbling fluidized bed with immersed vertical U-tube banks. *Chem. Eng. J.* 287, 727–743. doi:10.1016/j.ces.2015.11.049.
- Verma, V., Padding, J.T., Deen, N.G., Kuipers, J.A.M.H., Barthel, F., Bieberle, M., Wagner, M., Hampel, U., 2014. Bubble dynamics in a 3-D gas-solid fluidized bed using ultrafast electron beam X-ray tomography and two-fluid model. *AIChE J.* 60, 1632–1644. doi:10.1002/aic.14393.
- Werther, J., 2007. Fluidized-bed reactors. In: *Ullmann's Encyclopedia of Industrial Chemistry*, Wiley 723–725. doi:10.1002/14356007.b04\_239.pub2.
- Whitehead, A.B., Dent, D.C., Bhat, G.N., 1967. Fluidisation studies in large gas-solid systems Part I: bubble rise rates. *Powder Technol.* 1, 143–148. doi:10.1016/0032-5910(67)80025-1.
- Whitmarsh, E.A., Escudero, D.R., Heindel, T.J., 2016. Probe effects on the local gas holdup conditions in a fluidized bed. *Powder Technol.* 294, 191–201. doi:10.1016/j.powtec.2016.02.035.